

# Predictability of SST forced climate signals in two atmospheric general circulation models

X.-Z. Liang<sup>1</sup>, K.R. Sperber<sup>2</sup>, W.-C. Wang<sup>1</sup>, A.N. Samel<sup>1</sup>

<sup>1</sup>Atmospheric Sciences Research Center, State University of New York, Albany, New York, USA

<sup>2</sup>Program for Climate Model Diagnosis and Intercomparison, Lawrence Livermore National Laboratory, Livermore, California, USA

Received: 25 April 1996 / Accepted: 9 December 1996

**Abstract.** The predictability of atmospheric responses to global sea surface temperature (SST) anomalies is evaluated using ensemble simulations of two general circulation models (GCMs): the GENESIS version 1.5 (GEN) and the ECMWF cycle 36 (ECM). The integrations incorporate observed SST variations but start from different initial land and atmospheric states. Five GEN 1980–1992 and six ECM 1980–1988 realizations are compared with observations to distinguish predictable SST forced climate signals from internal variability. To facilitate the study, correlation analysis and significance evaluation techniques are developed on the basis of time series permutations. It is found that the annual mean global area with realistic signals is variable dependent and ranges from 3 to 20% in GEN and 6 to 28% in ECM. More than 95% of these signal areas occur between 35°S–35°N. Due to the existence of model biases, robust responses, which are independent of initial condition, are identified over broader areas. Both GCMs demonstrate that the sensitivity to initial conditions decreases and the predictability of SST forced responses increases, in order, from 850 hPa zonal wind, outgoing longwave radiation, 200 hPa zonal wind, sea-level pressure to 500 hPa height. The predictable signals are concentrated in the tropical and subtropical Pacific Ocean and are identified with typical El Niño/Southern Oscillation phenomena that occur in response to SST and diabatic heating anomalies over the equatorial central Pacific. ECM is less sensitive to initial conditions and better predicts SST forced climate changes. This results from (1) a more realistic basic climatology, especially of the upper-level wind circulation, that produces more realistic interactions between the mean flow, stationary waves and tropical forcing; (2) a more vigorous hydrologic cycle that amplifies the tropical forcing signals, which can exceed internal variability and be more efficiently transported from the forcing region. Differences between the models and observations are identified. For GEN during El Niño, the convection does not carry energy to

a sufficiently high altitude, while the spread of the tropospheric warming along the equator is slower and the anomaly magnitude smaller than observed. This impacts model ability to simulate realistic responses over Eurasia and the Indian Ocean. Similar biases exist in the ECM responses. In addition, the relationships between upper and lower tropospheric wind responses to SST forcing are not well reproduced by either model. The identification of these model biases leads to the conclusion that improvements in convective heat and momentum transport parametrizations and basic climate simulations could substantially increase predictive skill.

## 1 Introduction

The predictability of climate change forced by sea surface temperature (SST) anomalies has been a central issue in the study of intraseasonal to interannual variability. This topic has become a focus for increasing research activity because of two recent developments. First, simple and hybrid coupled ocean-atmosphere models demonstrate substantial skill in the forecast of tropical Pacific SST anomalies a year ahead of large El Niño/Southern Oscillation (ENSO) events (Zebiak and Cane 1987; Barnett et al. 1993). Second, atmospheric general circulation models (GCMs) show the ability to reproduce prominent circulation patterns in response to tropical Pacific SST anomalies (Fennessy and Shukla 1991; Lau and Nath 1994; Graham et al. 1994). These encouraging results have fostered the use of a two-tiered approach (Bengtsson et al. 1993; Barnett et al. 1994) and fully coupled GCMs (Latif et al. 1993; Ji et al. 1994) to produce potential long-range global climate predictions.

There are two general problems identified with the application of GCMs in the reproduction of SST induced climate changes. First, in contrast to highly predictable tropical SST anomalies and low latitude atmospheric responses, the relationship between extratropical atmospheric and land-surface variations and global SST forcing is difficult to determine (Palmer and Anderson 1994). This is attributed to the controlling effect of internal

atmospheric variability in the extratropics (Fennessy and Shukla 1991; Barnett et al. 1994; Harzallah and Sadourny 1994; Hoerling and Ting 1994). Second, current models still have substantial biases in their basic climatology simulations (Boer et al. 1992; Liang et al. 1995a), while GCM responses to SST anomalies are found to be strongly sensitive to the model climatology (Palmer and Mansfield 1986; Meehl and Albrecht 1991; Kumar et al. 1996). Therefore, both ensemble simulations with independent initial conditions and the use of different GCMs are necessary to identify robust SST signals from natural variability that are not model specific.

Several studies have addressed the identification of climate signals caused by external forcings (such as SST anomalies) versus natural variability (or climate noise) generated by internal atmospheric dynamics. The former can potentially be predicted with a knowledge of external anomalies while the latter is inherently unpredictable. The quantitative investigation on potential predictability pioneered by Madden (1976) used long records of observations to separate signals from noise by invoking the analysis of variance ratio between interannual variations and daily weather fluctuations. A similar approach was taken by Shukla and Gutzler (1983). Chervin (1986) proposed a different procedure, where the natural variability was measured by the interannual variance of seasonal means resulting from an extended GCM integration in the absence of nonseasonal external perturbations. As such, simulated and observed interannual variability were compared to determine that portion of the observed variance which is predictable. A third method was to compare a parallel pair of GCM simulations, where the first is forced by observed transient SST anomalies while the second prescribes the SST climatology for the identical period (Lau 1985; Chervin 1986). The enhanced variance from this forcing was then attributed to the predictable signals.

The validity of the first approach is built upon the assumption that interannual variability of monthly or seasonal means can be separated into unpredictable short time scale fluctuations and predictable longer time scale variations, while for the second and third methods it is assumed that the natural or externally forced variability in the real climate system is identical to those from GCM simulations. Both assumptions, however, are problematic. Zwiers (1987) showed that a large fraction of the interannual variance simulated in a GCM was potentially predictable but resulted from nonstationarity due to internal dynamics. We will demonstrate that, as a result of the existence of GCM climate biases, model-generated internal variability substantially differs from observations. In addition, all previous studies have relied upon the analysis of the variance ratio, which is the only statistical tool available for assessing potential predictability using a single realization of observations or GCM simulations (Zwiers 1987). The significance evaluation for this analysis, i.e., the *F-test*, requires a specification of the degrees of freedom and a normal distribution, both of which are not known *a priori*. Liang et al. (1995b) have discussed the drawbacks when the *F-test* is applied in a comparison of interannual variability, especially for short data records.

Given the scientific issues and statistical limitations discussed we believe that ensemble simulations of multiple GCMs can better be used to discern externally forced signals from climate noise produced by internal dynamics. The use of ensemble simulations also allows us to develop a new statistical methodology which consists of correlation analysis and significance evaluation techniques. Therefore, the purpose of this study is to evaluate the predictability of atmospheric responses to global SST anomalies using the ensemble simulations of two GCMs. These integrations (defined in Sect. 2) adopt “perfect” oceans where SST variations correspond to observations. This study is a necessary pre-requisite to any investigation of the potential predictive value of these models when they are coupled with interactive dynamic oceans. Model to observation and individual model run comparisons will be performed to identify robust SST forced climate signals from internal variability. Results from both GCMs are compared to investigate the predictability dependence on the model basic climatology.

After a brief description of the model formulations and observed data, the basic climatologies of both GCMs are compared with observations in Sect. 2. Correlation analysis and significance evaluation techniques are developed in Sect. 3. Section 4 investigates gross model predictability for the entire integration period and identifies signal regions where realistic simulations occur. This is followed, in Sect. 5, by cross validations of model capability to reproduce observed intraseasonal to interannual evolution of climate processes over these signal regions. Section 6 focuses on extreme anomaly teleconnections when intense ENSO events are observed. Finally we conclude with a summary of the work.

## 2 Model simulations and observed data

In this study, ensemble simulations from two GCMs (hereafter distinguished by GEN and ECM) are compared with each other and observations. The GEN is the GENESIS version 1.5 model that incorporates three major changes into the version 1.0 developed by Thompson and Pollard (1995): (1) the infrared radiation scheme is modified to include the effects of CH<sub>4</sub>, N<sub>2</sub>O, CFCI<sub>3</sub> and CF<sub>2</sub>Cl<sub>2</sub> (Wang et al. 1991); (2) atmospheric ozone is updated with TOMS, SAGE II and ozonesonde measurements to include longitudinal variations (Wang et al. 1995); (3) a new parametrization of fractional cloud cover and cloud radiative properties is developed to improve cloud-radiative forcing (Liang and Wang 1995). The ECM is the ECMWF cycle 36 model. The basic model dynamics and physical parametrizations are described in Simmons et al. (1988) and Tiedtke et al. (1988). The specified cycle uses the convection scheme of Tiedtke (1989) and the radiation schemes of Morcrette (1990, 1991). The more recent radiation schemes improve solar and infrared clear sky heating profiles that produce greater destabilization of the tropical atmosphere and, consequently, a much more vigorous hydrological cycle. Given these specifications, interested readers are referred to Phillips (1994) for more comprehensive GEN and ECM formulation documentation.

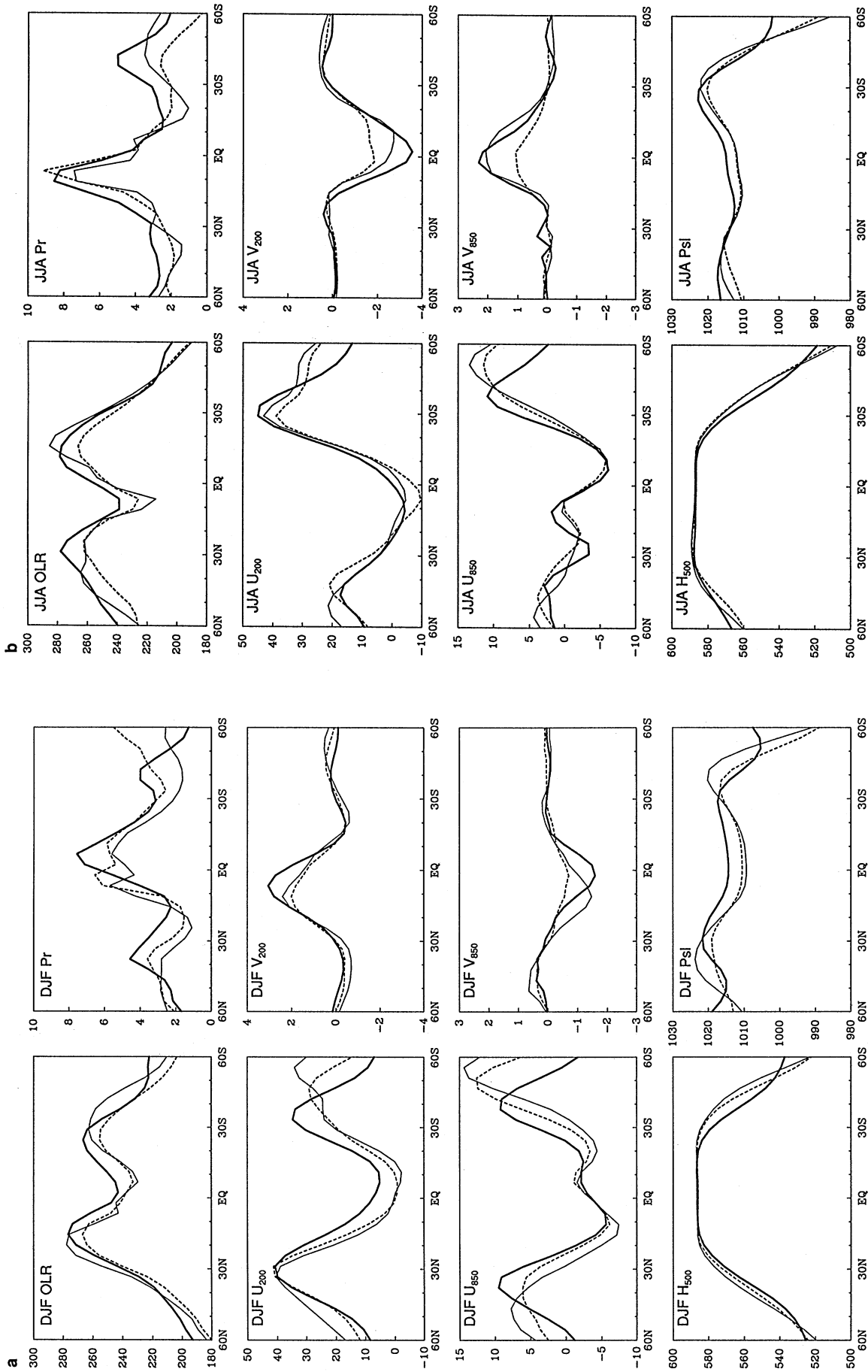


**Fig. 1a, b.** Latitudinal variations of **a** winter (DJF) and **b** summer (JJA) zonal mean circulations for observations (thin solid line), GEN (thick solid line), and ECM (thin solid line). The units are  $\text{W m}^{-2}$  for OLR,  $\text{ms}^{-1}$  for wind components (U: zonal; V: meridional), 10 m for H<sub>500</sub>, hPa for Ps, and  $\text{mm day}^{-1}$  for Pr (precipitation)

Five GEN simulations are carried out for the period 1979–1992 while the ECM is integrated six times for 1979–1988. Each of these independent realizations is initiated from a different set of atmospheric and land surface conditions. The initial state for the first ECM run is from the 15 January 1979 ECMWF operational analysis, while for GEN it is the 1 January restart condition from an earlier experiment with the same model where climatological SSTs were used. For both models, the final conditions from each run are used to initialize the subsequent run. All runs adopt the Atmospheric Model Intercomparison Project (AMIP) standard (Gates 1992). First, daily sea surface temperature and sea-ice cover variations are prescribed globally, where a linear interpolation from observed monthly mean distributions is used. For the period 1979–1988, the AMIP SST and sea-ice data set (see Gates 1992) is employed in both GCMs. The 1989–1992 values are obtained from the NOAA blended analysis (Reynolds and Marsico 1993). Note that both data sets are provided by the blended analysis from January 1982 onward. Second, the GCMs use an identical solar constant and CO<sub>2</sub> concentration. All other input parameters depend on the individual models (Phillips 1994).

Therefore, for a given GCM, individual runs differ only by their initial states. Each initial state retains complete balance between model processes that are constrained by sea surface conditions in the designated experiments. When the January 1979 sea surface anomalies are imposed to restart each run, perturbations occur and the model requires sufficient time to achieve a new balanced state. Thus, 1979 is used as a spin-up period and is not subject to analysis.

In this study we focus on variations in outgoing long-wave radiation (OLR), 200/850 hPa zonal wind ( $U_{200}/U_{850}$ ), 500 hPa height ( $H_{500}$ ) and sea-level pressure (Psl). These fields are most often used to represent large-scale circulation changes associated with ENSO. Note that OLR is directly related to cloud top temperature and thus a proxy for deep convection. High and cold cloud tops associated with deep convection emit less OLR. Hence, positive and negative OLR anomalies indicate suppressed and enhanced convection, respectively.

For comparison, observations between 1980–1992 are considered to be a single realization. The ECMWF analysis provides winds and geopotential heights at multiple atmospheric levels as well as sea level pressures (Trenberth 1992). Due to breaks in the data record, we choose to use a combination of the 1980–1984 WMO and 1985–1992 WCRP I archives. Note that Trenberth has identified several discontinuities in this hybrid data set. The OLR data are from NOAA measurements (Gruber and Krueger 1984).

The horizontal resolution is R15 ( $\sim 4.5^\circ$  latitude by  $7.5^\circ$  longitude) for GEN and T42 ( $\sim 2.8^\circ$  latitude by  $2.8^\circ$  longitude) for ECM. The ECMWF analysis is available on the T42 mesh while NOAA OLR data are archived at  $2.5^\circ \times 2.5^\circ$  regular intervals. In the current comparison, we choose to use the R15 grid, to which the higher resolution data are linearly interpolated.

Figure 1 illustrates observed and GCM simulated winter (December–January–February) and summer (June–July–August) zonal mean circulations averaged over the

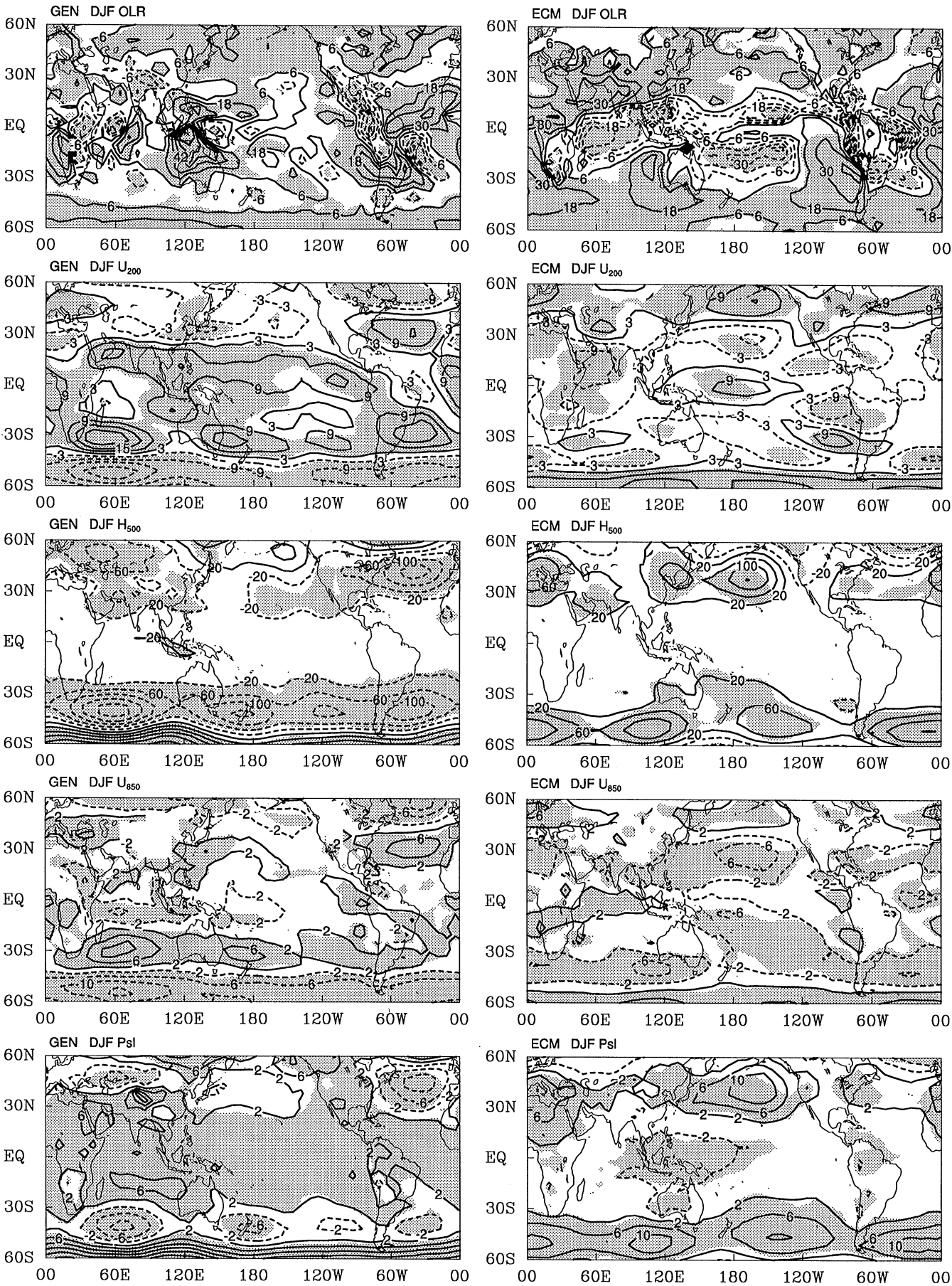
common period 1980–1988. In addition to the five selected variables, precipitation and meridional wind components at 200/850 hPa ( $V_{200}/V_{850}$ ) are also presented. The observed precipitation distribution is from Legates and Wilcott (1990). The model results are given as the ensemble means over all runs. Due to the fact that SST climate signals cannot be identified over the high latitudes (see Sect. 4), all latitudinal and geographic distributions are plotted between  $60^\circ\text{S} - 60^\circ\text{N}$ .

Clearly, when compared with GEN, ECM produces an overall better zonal mean climate between approximately  $30^\circ\text{S} - 30^\circ\text{N}$ , especially for the dynamic fields  $U_{200}$ ,  $V_{200}$ ,  $H_{500}$  and Psl. Over this latitudinal domain, GEN substantially overestimates Psl (weaker low) and  $U_{200}$  (reduced easterlies) throughout the year, while for  $V_{200}$ , it reveals stronger southerlies in winter and northerlies during summer. These biases indicate that GEN has an enhanced Hadley meridional circulation and a decreased east–west tropical Walker circulation. ECM also has a more realistic OLR distribution in the tropics and subtropics, while GEN generally underestimates convective activity. This is contrary to precipitation differences: for all months GEN produces greater rainfall but larger OLR (less cloud) than ECM. Although the lack of concurrent measurements makes it difficult to determine which model simulation of precipitation is more realistic, ECM is likely to generate a stronger cloud radiative forcing in correspondence to an equal amount of precipitation.

Substantial wind biases at 850 hPa exist in both GCMs. During winter, ECM (GEN) has large easterly (westerly) biases in mid-latitudes. Similar errors occur in the Southern Hemisphere mid-latitudes during summer. In the tropics and subtropics, both models produce much stronger northerlies in winter and southerlies during summer. This indicates a general overestimation of low-level meridional return flow associated with the enhanced Hadley circulation. Note that a large phase shift in winter  $V_{850}$  appears in ECM while it is realistic for GEN. Over higher latitudes ( $35^\circ$  poleward), GCM performance is overall poor, where GEN and ECM bias signs are often reversed. In particular, for GEN, both  $U_{200}$  and  $U_{850}$  reveal that the mid-latitude westerly jets during winter systematically shift equatorward, especially in the Southern Hemisphere. Accordingly, the GEN  $H_{500}$  and Psl values are substantially smaller (larger) in the mid-latitudes (high latitudes). These biases are essentially reversed in ECM.

Figure 2 depicts geographic distributions of winter model biases (GCM simulations minus observations) averaged over 1980–1988 for the five selected variables. Again, the model results represent the ensemble means over all runs. The statistical significance of the biases is given at the 99.9% confidence of a *Student's t*-test, assuming that the individual winters are independent. Small biases are indicated by those that are not statistically

**Fig. 2.** Geographic distribution of GEN and ECM model biases (differences between the simulations and observations) in winter circulations. Negative values are dashed. The contour intervals/reference contours are  $12/6 \text{ Wm}^{-2}$  for OLR,  $6/3 \text{ ms}^{-1}$  for  $U_{200}$ ,  $40/20 \text{ m}$  for  $H_{500}$ ,  $4/2 \text{ ms}^{-1}$  for  $U_{850}$  and  $4/2 \text{ hPa}$  for Psl. The shaded areas indicate biases that are statistically significant (see text)



significant. In addition to the zonal mean biases identified the following zonally asymmetric features are readily seen:

**OLR.** Both models show small errors in the tropical Pacific, but significant biases over central America (too much convection), most of the Atlantic Ocean and the west coasts off South America and Australia (too little cloud). GEN is also realistic over the central/east Pacific (180–100°W) and a strip extending from North Africa to India. In contrast, ECM is generally in error over these regions, where deep convection is much enhanced. For southeast Asia, ECM is reasonably accurate while GEN generates much less convection and a weak Australian monsoon.

**$U_{200}$ .** A realistic wind distribution over the east Pacific Ocean (except the GEN equator) is simulated in both models. The tropical easterlies in GEN are too weak and limited in coverage. In contrast, the ECM errors are generally small over most tropical and subtropical regions.

**$H_{500}$ .** Over the North Atlantic Ocean, GEN has an amplified trough while ECM is more realistic. The northwest Pacific trough is accurate in GEN but too weak in ECM. The tropical and sub-tropical biases are generally not significant in either model, although GEN has higher heights near Indonesia.

**$U_{850}$ .** GEN is realistic over most of the Pacific Ocean while it shifts the North Atlantic westerly jet to the south. In contrast, ECM shifts the North Pacific westerly jet to the north but better simulates the North Atlantic Ocean field. Both models produce realistic values over the tropical Pacific.

**Psl.** GEN better simulates the Aleutian low over the North Pacific Ocean but shifts the Atlantic low to the south. Both of these features resemble the  $U_{850}$  pattern. ECM biases are opposite to those of GEN over these regions. In the tropics and extratropics, GEN produces systematically higher pressures, while ECM is generally realistic, except over southeast Asia/west Pacific Ocean where the low center is deeper.

Note that the winter climate biases in GEN and ECM resemble the observed anomaly signatures that are associated with El Niño and La Niña phenomena, respectively. Figure 3 shows the zonal mean winter Psl biases. When compared with van Loon and Madden (1981; Figs. 7 and 13), the ECM errors resemble the composite anomalies where extremely low pressures occur over the tropical central/east Pacific and heavy rainfall is observed over the equatorial Pacific, while the GEN errors are reversed and correspond to the opposite events.

In summary, the basic climates of both GCMs are substantially different from observations over several broad regions. Both models significantly overestimate low-level meridional flow associated with the enhanced Hadley circulation. The mid-latitude westerly jets during winter systematically shift equatorward in GEN and poleward in ECM. The GEN OLR underestimates

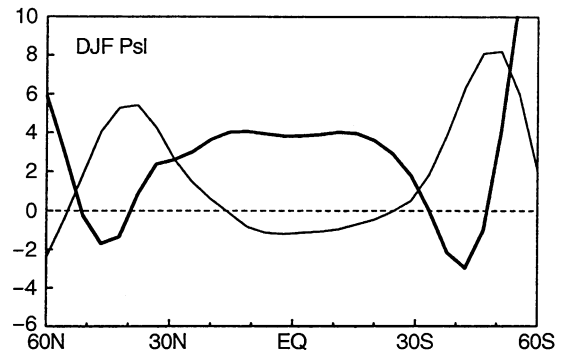


**Fig. 3.** Latitudinal variations of GEN (thick solid line) and ECM (thin solid line) model biases in zonal mean winter Psl (hPa)

cloud-radiative forcing associated with tropical convective activity, while an overestimation occurs in ECM. In general, ECM better simulates the dynamic variables ( $U_{200}$ ,  $V_{200}$ ,  $H_{500}$ , Psl), especially in the zonal mean circulation between 30°S–30°N. ECM also produces more realistic zonal mean OLR variations in the tropics and subtropics, although large errors are found in the longitudinal distribution. The ECM low-level wind simulation, however, is somewhat worse than GEN. These biases may constrain GCM capability to achieve SST forced climate predictability (Palmer and Mansfield 1986; Meehl and Albrecht 1991; Kumar et al. 1996) and, therefore, will be considered when the findings are interpreted later.

### 3 Methodology

Given any two time series at a specific location with  $L$  records, i.e.,  $F_k = \{F_{kl}; l = 1, 2, \dots, L; k = i \text{ or } j\}$ , the mean and covariance are calculated as follows:

$$\bar{F}_k = \frac{1}{L} \sum_{l=1}^L F_{kl}, \quad k = i \text{ or } j \quad (1)$$

$$C_{ij} = \frac{1}{L} \sum_{l=1}^L (F_{il} - \bar{F}_i)(F_{jl} - \bar{F}_j) \quad (2)$$

The pointwise correlation between the two series is then obtained as:

$$R_{ij} = C_{ij} / \sqrt{C_{ii} \cdot C_{jj}} \quad (3)$$

where  $C_{kk}$  is the variance for series  $k$  and is evaluated by setting  $i = j = k$  in Eq. (2). To measure the relationship between observations and the GCM simulations, an ensemble mean correlation is constructed using all  $M$  runs:

$$R_{oe} = \frac{1}{M} \sum_{m=1}^M R_{om} \quad (4)$$

where subscripts  $o$  and  $m$  denote, respectively, observations and model runs. Similarly, an ensemble mean correlation can also be constructed using all distinct

combinations of  $M$  runs to measure the inherent coherence between individual model simulations:

$$R_{me} = \frac{1}{N} \sum_{i=1}^{M-1} \sum_{j=i+1}^M R_{ij}, \quad N \equiv \sum_{i=1}^{M-1} (M-i) = \frac{M \cdot (M-1)}{2} \quad (5)$$

Recall that the ECM results are available during 1980–1988, which is shorter than the GEN and observed period 1980–1992. Hence, in Sect. 4, the ECM  $R_{oe}$  and  $R_{me}$  are calculated during 1980–1988 with  $L = 9$  and  $M = 6$ , while the GEN values are for 1980–1992 with  $L = 13$  and  $M = 5$ . In the comparison of interannual evolution (Sect. 5) and extreme anomalies (Sect. 6), however, the common period 1980–1988 averages are used as the reference climatology to construct the observed and simulated anomalies.

One important issue that must be addressed in this study is the identification of robust climate signals that are forced by SST anomalies. Liang et al. (1995b) developed a climate ensemble technique to compare interannual variability. This technique determines statistical significance by using the empirical probability distribution generated from a resampling procedure. The accessibility of much longer data records (i.e., 40 to 100 y) made this determination possible by generating permutations of all contiguous sub-periods of a fixed length. In the current study, the data records are not sufficiently long. The availability of an ensemble of GCM runs that uses different initial conditions, however, enables a similar resampling procedure to be developed. Since the SST variations in all model runs correspond to observations, robust climate signals that result from this surface forcing must be dominantly manifested in correlations  $R_{oe}$  and  $R_{me}$ , where the indices  $\{l\}$  in Eqs. (1)–(2) are in sequential order according to the calendar year. Otherwise, the responses are likely generated by chance. Thus, one equivalent significance test is to evaluate the importance of this sequential order. In this case the original time series of a reference run is reserved while the resampling procedure generates random permutations (without replication) from the time series of the remaining runs. These reordered sets, which consist of all original values, are then used with the reference run to calculate correlation coefficients. This step is repeated for each run such that the full set of permutations is based on  $N$  combinations of  $M$  runs (Eq. (5)) for each GCM. Finally, the resulting coefficients are used to construct the correlation probability distribution.

This study uses 1000 permutations. The correlation probability distribution is constructed for each climate variable at individual grid points. Figure 4 shows global area means and standard deviations of the pointwise cumulative probability as a function of correlation threshold. The calculation is based on all calendar months and all selected variables. This probability equals the percentage of permutations that have  $R_{ij}$  values less than the threshold. Clearly, the deviations are not negligible so that pointwise thresholds must be applied for each field. This arises because of temporal autocorrelation that is both region and variable specific. It is thus difficult to apply traditional statistic tests (such as *Student's t*) for

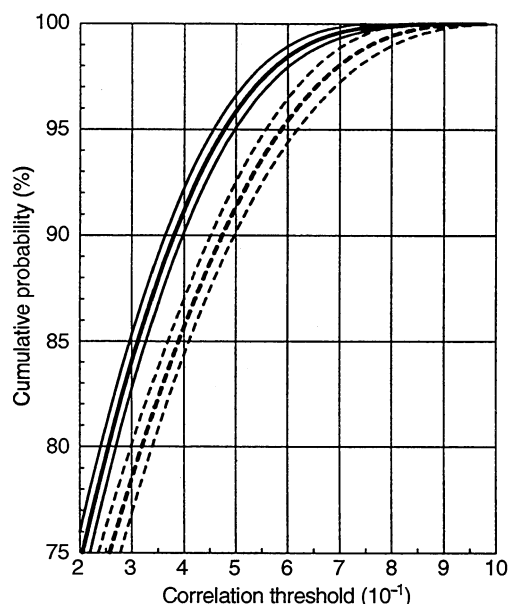


**Fig. 4.** Global area means and standard deviations of the pointwise cumulative probability as a function of correlation threshold (see the text) for GEN (solid) and ECM (dashed). Means are shown by thick curves while  $\pm 1$  deviations by thin curves

correlation significance, since they require a specification of the degrees of freedom and a normal distribution, both of which are not known *a priori*. Note that the number of elements (i.e., years) in a series has a systematic effect on the distribution. GEN has five independent runs of 13 y, while ECM has six integrations of 9 y. Hence, GEN has a larger number of degrees of freedom. As a result, a comparatively smaller correlation threshold is needed for GEN to achieve a same confidence level as ECM. Here we choose the 90% confidence level for significant tests. The corresponding mean correlation thresholds are 0.381 for GEN and 0.473 for ECM. The ratio of the two mean values is used to scale the ECM  $R_{oe}$  contour maps in Sect. 4 for visual compatibility with the GEN plots.

This procedure also addresses the “field significance” issue raised by Livezey and Chen (1983). This is caused by the non-trivial effects of number and interdependence when the collective significance of finite sets of statistics is evaluated. In our case, this measure can be estimated with the permutation procedure described already. However, the fractional area of any given domain is integrated, where local correlation coefficients in each reordered permutation map are identified as significant at the 90% confidence level. These integrated values for 1000 permutations result in an empirical distribution, which is used to determine the probability that the fractional area of the domain having by chance significant correlation coefficients exceed the corresponding values on the  $R_{me}$  or  $R_{oe}$  maps. This probability is reported as the field significance.

Note that  $R_{oe}$  and  $R_{me}$  are used to measure model performance (compared with observations) and inherent coherence between ensemble runs over the entire integration period. For the individual year comparisons discussed in Sect. 6, a measure of coherence between

anomalies of ensemble simulations is necessary, not only to indicate the signal robustness but to avoid producing a massive number of maps for individual runs. For a specific year  $l$ , one such measure is:

$$Cc = \frac{\sum_{i=1}^{M-1} \sum_{j=i+1}^M (A_{il} \cdot A_{jl} + A_{jl} \cdot A_{il})}{\sum_{i=1}^{M-1} \sum_{j=i+1}^M (A_{il} \cdot A_{il} + A_{jl} \cdot A_{jl})} \quad (6)$$

where anomalies  $A_{kl}$  equal departures of  $F_{kl}$  from the 1980–1988 climatology mean. Similar to the correlation coefficient,  $Cc$  varies from  $-1$  to  $+1$ .

One remaining problem is the determination of the  $Cc$  threshold, above which individual runs show a coherent anomaly signal. Since the concern is with extreme anomalies, we shall focus on regions where ensemble mean anomaly magnitudes deviate by more than one standard deviation from the 1980–1988 climatology. Figure 5 shows the cumulative probability as a function of  $Cc$  threshold for GEN and ECM. The calculation is based on all calendar months and all variables over regions where extreme ensemble mean anomalies are identified. This probability indicates the percent area where anomalies from the individual realizations are less than 0.0, 0.5, 1.0 standard deviations. Note that the anomalies from each run are *a priori* reversed in sign when the ensemble mean value is negative. Clearly, when the threshold increases, the individual run fluctuations from the ensemble mean decrease. For simplicity, we choose a uniform 0.5 as the  $Cc$  threshold for both GEN and ECM. When  $Cc$  values are larger than this threshold, the probability that individual runs produce the incorrect anomaly sign is overall less than 2%, while that for

anomaly magnitudes smaller than one half deviation is less than 6%.

We shall emphasize that, for all results reported here, the statistical techniques are first applied to individual calendar months. These monthly outputs are then used to obtain seasonal or multiple-month running means. As demonstrated by Kiladis et al. (1994) and Meehl et al. (1996), tropical-mid-latitude interactions are often associated with two major time scales: submonthly (less than 30 days) and intraseasonal (30–70 days). The use of monthly samples effectively eliminates the contribution from submonthly fluctuations, while the intraseasonal factor is retained in the seasonal or multiple-month running mean results.

#### 4 Ensemble predictability

This section focuses on gross model predictability during the entire integration period (1980–1992 for GEN and 1980–1988 for ECM) by evaluating  $R_{me}$  and  $R_{oe}$  geographic distributions.  $R_{me}$  measures the relative contributions of internal and external variability and, hence, indicates the reproducibility of climate responses by a GCM when forced with observed sea surface variations. Due to the existence of significant model biases, however, highly reproducible model responses do not necessarily represent observed climate signals. On the other hand,  $R_{oe}$  shows the similarity of multiple simulations with a single observed realization. In this case, model deficiencies may generate internal variability that differs from natural variability and, thus,  $R_{oe}$  cannot entirely identify the observed climate signals that result from the surface forcing. Nevertheless,  $R_{oe}$  depicts the capability of the target model to simulate, partially, these signals.

Figure 6 shows the  $R_{oe}$  geographic distributions averaged over the winter (January, February, December) and summer (June, July, August) months. The statistically significant areas of  $R_{oe}$  and  $R_{me}$  are both illustrated. Recall that the seasonal averages are obtained from monthly  $R_{oe}$  or  $R_{me}$  analyses and that, for better compatibility with GEN, the ECM  $R_{oe}$  contours are scaled by a factor of 0.805 (0.381/0.473). Four important features are noted.

1. Both GEN and ECM  $R_{me}$  results indicate that internal variability is dominant while robust model responses, which are independent of initial condition, account for a small fraction of area. This fraction (where  $R_{me}$  is significant), when annually averaged over the globe, ranges from 5.2, 7.0, 10.9, 17.9 to 25.0% for GEN  $U_{850}$ , OLR,  $U_{200}$ , Psl,  $H_{500}$ , respectively. The corresponding values for ECM are 16.1, 18.9, 26.0, 34.0 and 38.1%. More than 95% of the significant areas are identified between 35°S and 35°N.

2. The area of significant  $R_{oe}$  is less extensive than that of  $R_{me}$ , which implies the impact of model biases. As discussed, only a portion of the robust model responses are realistic. For  $U_{850}$ , OLR,  $U_{200}$ , Psl,  $H_{500}$ , realistic signals are identified over 3.1, 5.0, 7.9, 8.1 and 19.8% of the total area in GEN and 6.3, 8.4, 11.2, 13.7, 28.0% in ECM. Again, more than 95% of these signal areas occur between 35°S and 35°N.

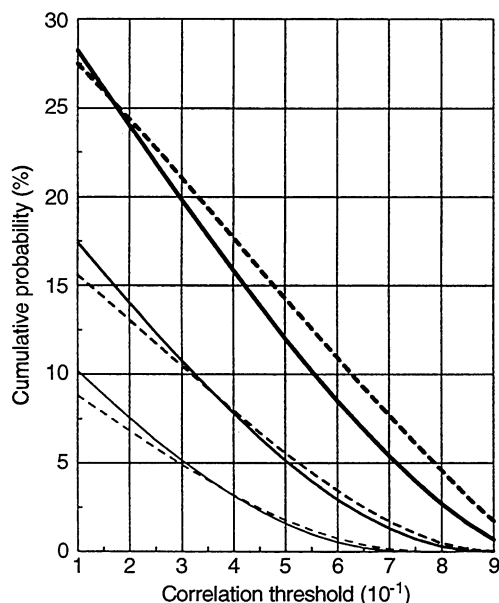


**Fig. 5.** The cumulative probability as a function of  $Cc$  threshold (see text) for GEN (solid) and ECM (dashed). Thin, medium and thick curves denote probability values for anomalies less than 0.0, 0.5 and 1.0 standard deviations



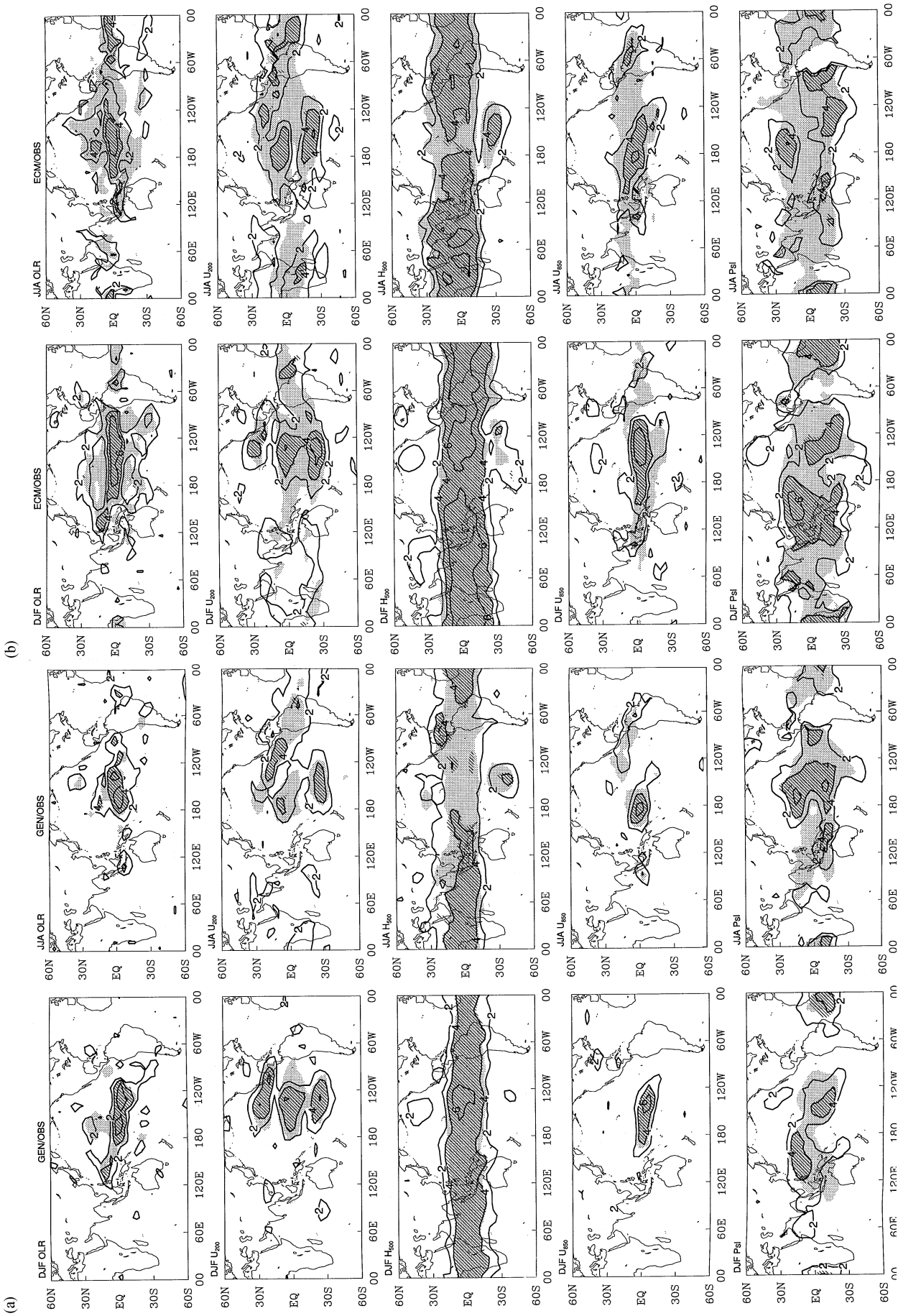


**Fig. 6a, b.**  $R_{oe}$  geographic distributions averaged during winter (DJF) and summer (JJA) months for a GEN and b ECM. Coefficients are multiplied by 10 where positive values are contoured at an interval of 2. The hatched and shaded areas indicate where  $R_{oe}$  and  $R_{me}$ , respectively, are statistically significant

3. ECM has broader areas of significant  $R_{me}$  and  $R_{oe}$  than GEN for each variable and, hence, exhibits less sensitivity to initial conditions and higher predictability of SST forced climate changes. For example, ECM shows robust signals, especially during summer, in the tropical Atlantic Ocean and adjacent land areas, while the GEN response, excepting  $H_{500}$ , is almost zero. Recall that ECM simulates a more realistic climatology (Figs. 1–2; see Sect. 2). It is asserted that a better basic climate simulation is associated with an improved response to SST forcing. This result reinforces previous findings by Palmer and Mansfield (1986), Meehl and Albrecht (1991) and Kumar et al. (1996). Note that the degree of sensitivity and predictability is variable dependent. Both models demonstrate that sensitivity decreases while predictability increases from  $U_{850}$ , OLR,  $U_{200}$ , Psl to  $H_{500}$ .

4. The simulation of realistic responses differs remarkably between variables. OLR signals are essentially confined to the equatorial central Pacific. Over this region, the SST periodically exceeds the approximate  $28^{\circ}\text{C}$  threshold required for the maintenance of organized convection (Graham and Barnett 1995). Both GCMs portray reasonably well the observed link between OLR and/or deep convection with SST anomalies.  $U_{200}$  exhibits three distinct core regions over the central/east Pacific where the signal is realistic. The two subtropical centers are symmetric to the equatorial strip and are located near  $25^{\circ}\text{S}$  and  $25^{\circ}\text{N}$ . These centers represent the most poleward robust responses among all selected variables and play an important role in the transfer of tropical signals to the extratropics. A broad zonal  $H_{500}$  signal occurs throughout the tropics. This feature is the result of a uniform atmospheric thermal response that dominates the tropics in both observations and the simulations (see Sect. 5).  $U_{850}$  signals are confined to the equatorial Pacific Ocean and are associated with the low-level convergence required for intense convection, which is well simulated. Two core regions are identified with the winter Psl field and are located over the Indo/Australian region and the southeast tropical Pacific Ocean. These signatures are all reminiscent of ENSO related phenomena, which are detailed in the following sections.

Figure 7 shows monthly variations in the fractional area with statistically significant pointwise  $R_{oe}$  values and the corresponding field significance (see Sect. 3). For the entire domain between  $35^{\circ}\text{S}$  and  $35^{\circ}\text{N}$ , the GEN field significance does not generally exceed the 90% level, except for  $H_{500}$ . In contrast, there are several months during which ECM Psl and  $U_{200}$  exceed this level. When the domain is limited in the Pacific portion ( $120^{\circ}\text{E}$ – $100^{\circ}\text{W}$ ), most months, especially in ECM, are identified with larger than 90% field significance. The result confirms that ECM has greater predictability than GEN. In addition,  $H_{500}$  for both models contains the most extensive signal while  $U_{850}$  has the least. Most of the realistic signals are confined to the Pacific, especially for  $U_{850}$  and OLR.

Performance differences between the two models are not likely to result from the use of different periods. Figure 8 shows temporal variations in the five-month running mean correlation skill score for the entire integration period. This score is calculated by Eq. (4), where the sample indices  $l$  represent all grid-point anomalies within the domain  $35^{\circ}\text{S}$ – $35^{\circ}\text{N}$ . These anomalies are based on the

1980–1988 climatologies for observations or individual GCM realizations. Clearly, during the common period, ECM has higher scores than GEN for all variables, especially when strong SST anomaly events occur. Note that the  $H_{500}$  scores are generally smaller than those for the other fields. This is not inconsistent with Fig. 6, since the dominant contribution of zonal mean variations is mostly removed during the spatial correlation calculation.

Recall that the GEN and ECM basic climate states have, respectively, El Niño- and La Niña-like biases (see Sect. 2). Thus, the transient SST anomaly forcing is superimposed on the basic states that have elements of the warm (GEN) and cold (ECM) events. One may argue that this contrast in basic states could explain model predictability differences. Examination of Fig. 8, however, does not support this explanation. For both GCMs, no systematic difference in the predictive skill is found between El Niño and La Niña events. A similar conclusion can be drawn from the result of Kumar et al. (1996; Fig. 2).

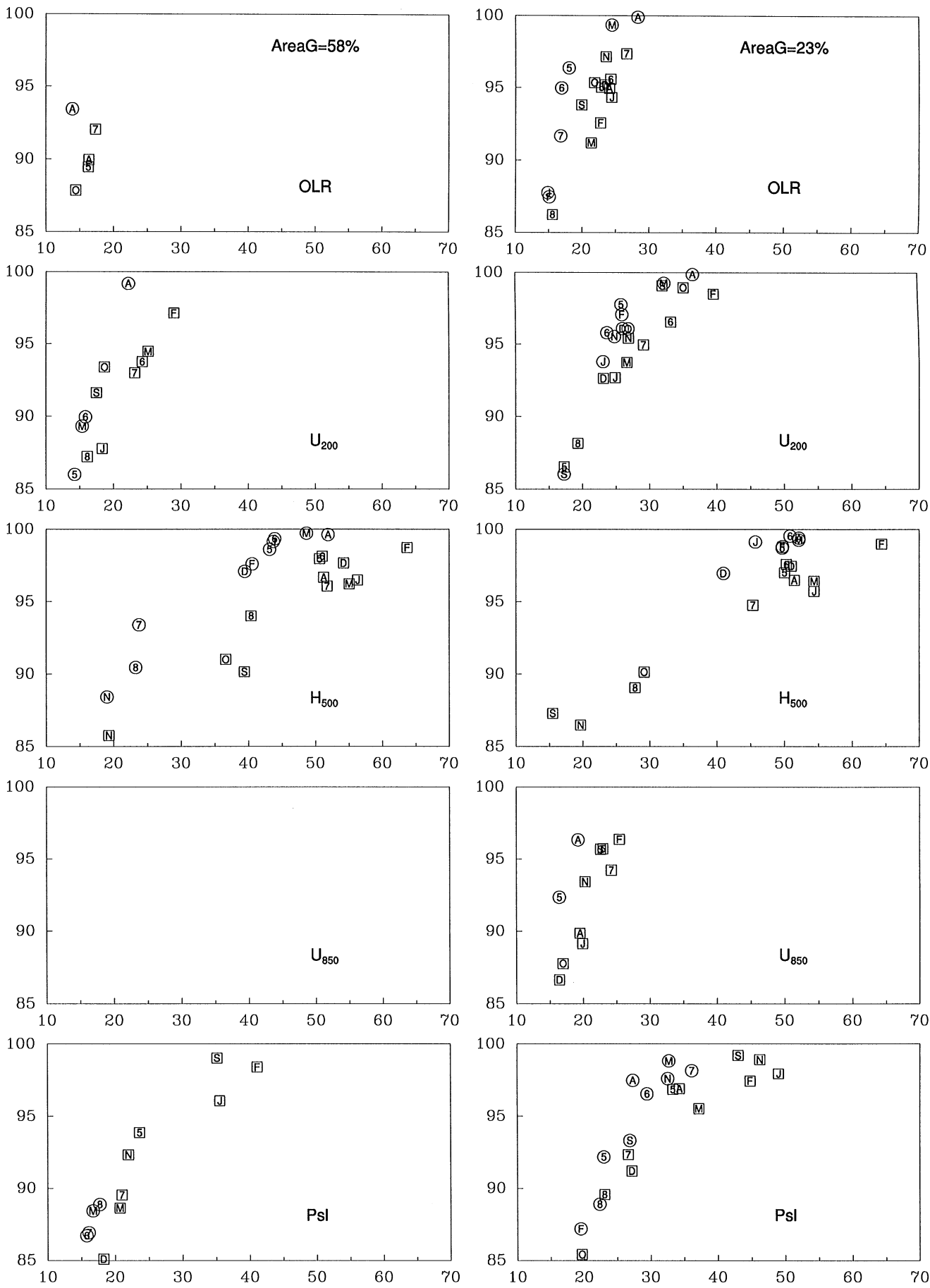
## 5 Interannual evolution

We now study the interannual evolution of circulation processes over the robust signal regions identified in Sect. 4. Examination and comparison of the actual time series offer a more intuitive test and interpretation of correlation significance. When compared with observations, the model results are hereafter presented as ensemble means of all individual runs.

### 5.1 Characteristic regional mean indices

Since realistic signals are identified primarily in the equatorial zone, we first study the interannual evolution of the tropical circulation. Based on the findings from the previous section, we show monthly variations in equatorial ( $5^{\circ}\text{S}$ – $5^{\circ}\text{N}$ ) averages for  $160^{\circ}\text{E}$ – $140^{\circ}\text{W}$  OLR,  $160^{\circ}\text{E}$ – $100^{\circ}\text{W}$   $U_{200}$ , zonal mean  $H_{500}$  and  $150^{\circ}\text{E}$ – $150^{\circ}\text{W}$   $U_{850}$  as well as the Southern Oscillation Index (SOI). Here, SOI is defined as the Psl difference between the average of the four grid points that surround Tahiti ( $149.6^{\circ}\text{W}$ ,  $17.5^{\circ}\text{S}$ ) and Darwin ( $130.9^{\circ}\text{E}$ ,  $12.4^{\circ}\text{S}$ ). These specified regions are identified with the most realistic simulations in both models, where  $R_{oe}$  is large and statistically significant. Similar regional indices are commonly used to represent ENSO related circulation features. Figure 9 illustrates observed and simulated five-month running mean anomalies of these quantities, where the respective 1980–1988 monthly climatological values are previously subtracted. For reference, observed equatorial east Pacific ( $150^{\circ}\text{W}$ – $90^{\circ}\text{W}$ ,  $5^{\circ}\text{S}$ – $5^{\circ}\text{N}$ ) SST anomalies are displayed in conjunction with the  $H_{500}$  plot.

**Fig. 7.** Monthly variations in the fractional area with statistically significant pointwise  $R_{oe}$  values (*abscissas*, %) and the corresponding field significance (*ordinates*, %) for the entire domain between  $35^{\circ}\text{S}$ – $35^{\circ}\text{N}$  (*left panels*) and the Pacific portion  $120^{\circ}\text{E}$ – $100^{\circ}\text{W}$  (*rights panels*). Symbols *J*, *F*, *M*, *A*, *5*, *6*, *7*, *8*, *S*, *O*, *N* and *D* denote the calendar months January to December, respectively. *Outline circles* indicate GEN results, while the *squares* represent ECM. The domain area percentage of the globe is also listed (*AreaG*)



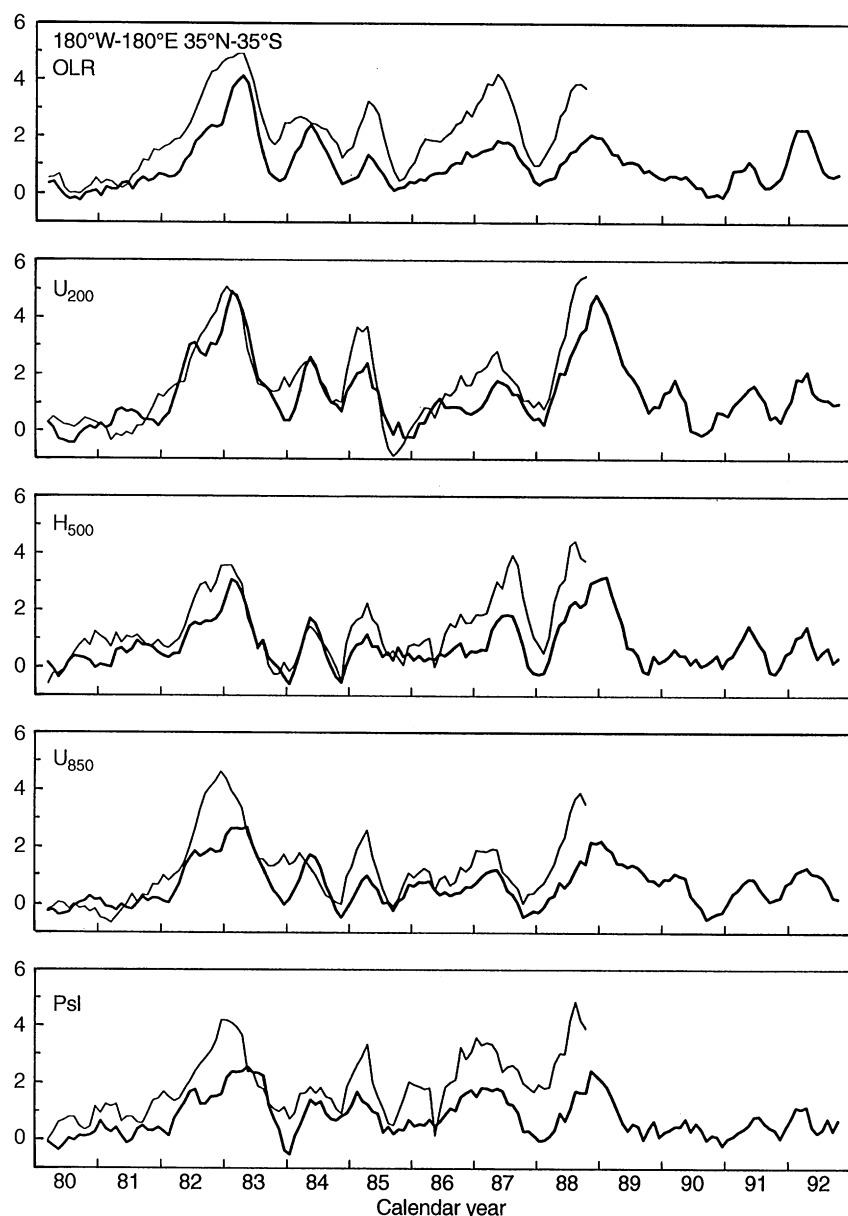


**Fig. 8.** Five-month running mean correlation skill scores ( $\times 10$ ) based on grid-point anomalies over  $35^{\circ}\text{S}$ – $35^{\circ}\text{N}$  for GEN (thick solid) and ECM (thin solid)

Figure 9 clearly portrays the tropical circulation variations associated with the ENSO life cycle. The integration period encompasses three warm episodes and one cold event: 1982/83, 1986/87 and 1991/92 El Niños, and the 1988/89 La Niña. A relatively weak cold phase occurred in 1984/85 and shares many similarities with the better defined case just listed. During a typical El Niño, positive SST anomalies are observed in the central and east tropical Pacific while they are opposite for a La Niña (Rasmusson and Carpenter 1982; Philander 1990). Given these SST anomaly characteristics, both GCMs successfully reproduce pertinent observed climatic responses. The response polarity reverses from El Niño to La Niña. In the case of El Niño, salient circulation changes over the central and east equatorial Pacific include a negative OLR anomaly, which indicates enhanced convection, diminished low-level easterly and upper-level westerly flow. In

addition, the east-west surface pressure gradient decreases (a negative SOI anomaly), where Psl falls in the southeast tropical Pacific and rises over the Indo/Australian region. Finally, a systematic positive  $H_{500}$  anomaly occurs throughout the entire tropical belt. This feature will be discussed later.

In spite of the general responses discussed, the simulations differ from observations in structure detail. First, ECM overestimates the OLR anomaly magnitude. This indicates a stronger model OLR response to deep convective activity, i.e., an enhanced longwave cloud-radiative forcing. Second, the simulation of the 1982/83 event is quite complicated. SOI comparisons indicate that the event occurs approximately one half year earlier in GEN than in observations. This phase shift, coupled with a smaller magnitude, is consistently seen in both the Tahiti and Darwin Psl anomalies as well as in OLR. A similar

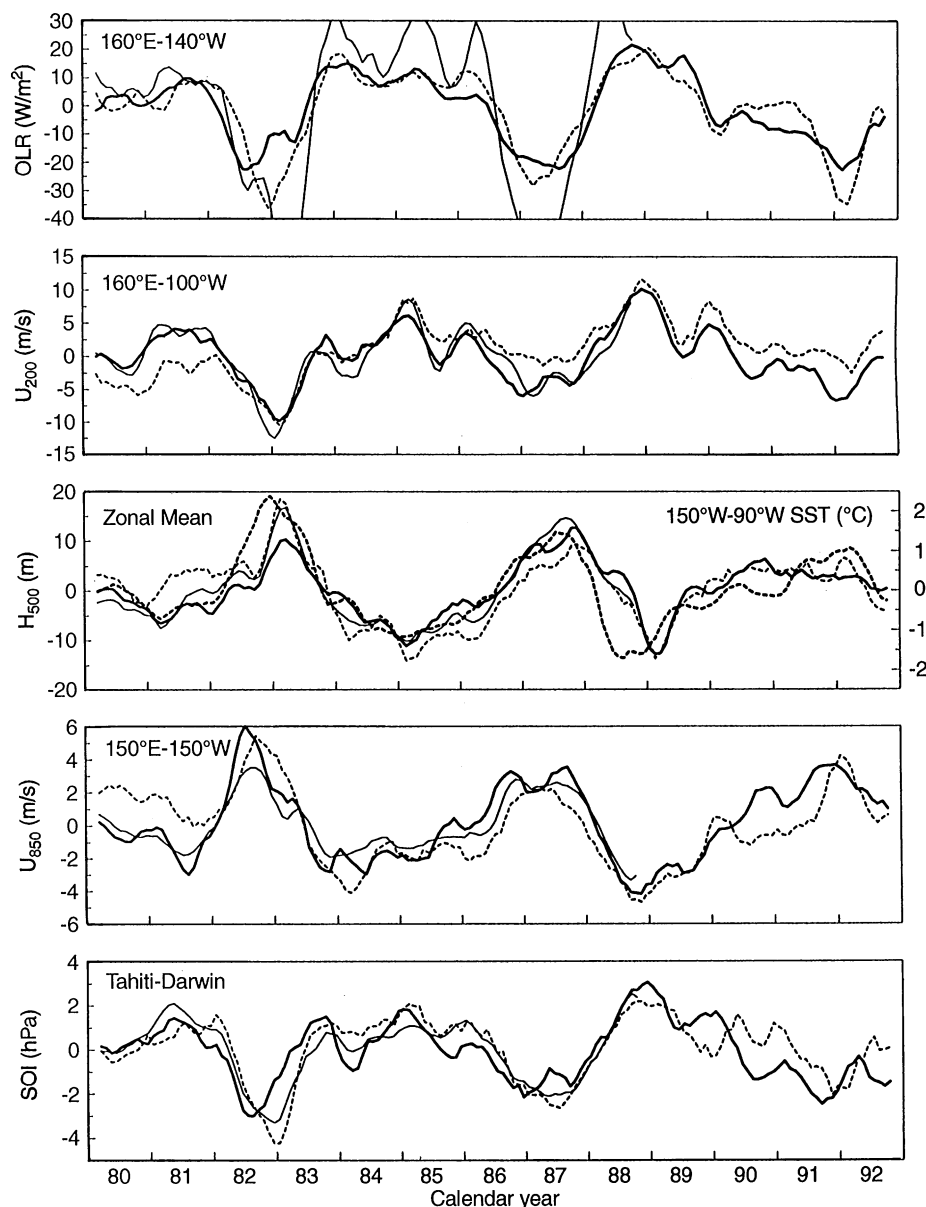


**Fig. 9.** Five-month running mean anomalies averaged over the equatorial belt ( $5^{\circ}\text{S}$ – $5^{\circ}\text{N}$ ) and specific longitudinal ranges (displayed in the upper-left corner of each plot) for observations (*thin dashed*), GEN (*thick solid*), and ECM (*thin solid*). Included with  $H_{500}$  is the observed equatorial east Pacific SST anomaly (*thick dashed*), where the scale and regional specification are on the right

shift occurs in  $U_{850}$ , although the magnitude is realistic. In contrast, accurate  $U_{200}$  evolution and correct phasing are produced. The zonal mean  $H_{500}$  amplitude, however, is too small. Little phase shift is evident in ECM, although the wind responses lead observations slightly. The ECM SOI anomaly is smaller than, but in phase with, observations. Two compensating factors produce this result: the Psl response is realistic near Darwin while, as in GEN, it is both weaker than and leads observations over Tahiti. In addition, ECM accurately simulates  $H_{500}$  evolution, whereas it underestimates the  $U_{850}$  anomaly magnitude. Third, both GCMs fail to reproduce observed variations during 1980–1981, where larger  $U_{200}$ , lower  $H_{500}$  and smaller  $U_{850}$  values are calculated systematically by the models (This failure may be related to ECMWF analysis data quality problems, Trenberth and Olson 1988). The anomaly bias signs are reversed during 1986–1987. The 1988–1989 simulation appears to be the most accurate.

These three periods happen to correspond, respectively, to normal, warm and cold ENSO phases. The 1990–1991 biases resemble those of 1986–1987.

## 5.2 Symmetric thermal response in the tropics

One striking feature associated with ENSO is the zonally symmetric response in the equatorial upper tropospheric geopotential height field. Figure 6 shows that both models realistically simulate interannual  $H_{500}$  variations throughout the tropics. When the zonal means of individual years are removed, however, no consistency between observations and simulations is evident from the  $R_{oe}$  and  $R_{me}$  analyses. This indicates the dominance of uniform  $H_{500}$  fluctuations in the tropics. Furthermore, Fig. 9 shows that, in the equatorial belt, both observed and simulated zonal mean  $H_{500}$  variations generally correspond to east Pacific SST fluctuations.

Several observational and GCM studies have found this feature to be a significant signal in the tropical circulation. Horel and Wallace (1981), based on radiosonde station data, showed that most 200 hPa height anomalies tend to be positive during El Niños and negative otherwise. This emphasizes the close link between tropospheric temperatures throughout the tropics and equatorial Pacific SSTs. Angell and Korshover (1983), Pan and Oort (1983) and Barnett (1985) further demonstrated that observed thermal surface anomalies extend upward with time. This indicates a lagged relationship between the upper tropospheric response and the surface forcing. This is also apparent in Fig. 9 during 1982–1983 and 1986–1989, when the east Pacific SST anomalies lead the zonal mean  $H_{500}$  responses by one to two seasons in both observations and simulations. This phase shift, however, is not obvious during other periods.

To depict the vertical structure of circulation changes associated with tropical SST forcing, composite longitude-altitude charts of  $5^{\circ}\text{S}$ – $5^{\circ}\text{N}$  mean geopotential height anomalies are constructed. Due to data availability, only the observed and GEN simulated heights at 1000, 850, 700, 500, 300, 200, 100 hPa are compared. The composites are based on the 1982/83, 1986/87 warm episodes and the 1984/85, 1988/89 cold phases. The 1991/92 event is excluded given the small zonal mean  $H_{500}$  anomalies in both observations and simulations (Fig. 9). Although anomalies differ quantitatively from event to event, the composite features described later are qualitatively representative. Figure 10 shows the three-month averaged composites of the four events, where the polarity of cold phase anomalies is reversed. Note that the winter composite represents the mean of December 1982, 1984, 1986, 1988 and the subsequent Januaries and Februaries. The composites from the preceding autumn (September, October, November) as well as the following spring (March, April, May) and summer (June, July, August) are also shown. For reference, the specified autumn, winter, spring and summer are traditionally regarded as, respectively, the antecedent conditions, the onset, peak and transition phases of warm episode (Rasmusson and Carpenter 1982).

In general, GEN reproduces the observed characteristic: a dipole structure near the surface that becomes a monopole signal in the free troposphere. Over the east Pacific core region, the anomalies in the planetary boundary layer (PBL) and the free troposphere are out of phase, i.e., a baroclinic response occurs. In contrast, a barotropic thermal response takes place along the rest of the equator. The transition between dipole and monopole is located near 700 hPa. This agrees with Barnett (1985), who suggested a level between 850 and 500 hPa. During the antecedent conditions, the warming is concentrated in the upper troposphere just above the positive SST anomaly.

This warming intensifies and overspreads the tropics during the onset phase. When the peak phase occurs, the signal is relatively large and is of near equal strength throughout the tropical belt. This feature is maintained in the transition phase, although anomaly magnitude decreases slightly. Note that the surface dipole response is evident during all four seasons. This is a signature of the Southern Oscillation as seen in Psl (see SOI in Fig. 9).

Important differences, however, are identified between observations and GEN. The GEN warming center is located at a lower altitude, although the longitudinal position is realistic. As a result, the model overestimates  $H_{500}$  anomalies. This is evident during both the 1982/83 and 1986/87 events (Fig. 9), and indicates that the model convection parametrization does not carry the lower level energy to a sufficiently high altitude. Meehl and Albrecht (1991) showed that the incorporation of a better convection scheme which, in the vicinity of the SST anomaly, transports heat and moisture higher into the troposphere, can enhance tropical heating and associated extratropical circulation anomalies. In addition, the spread of the warming along the equator is much slower and the anomaly magnitude smaller than observations. As a result, warming in the tropics away from the core region is only half of that observed throughout the entire one year period. This disparity may partially explain the absence of robust and realistic wind field responses over the Eurasian sector. Note that the warming above the core region is relatively accurate except during the transition phase. As a consequence, the meridional transport of heat and momentum seems to be adequate. This in turn leads to a successful simulation of circulation pattern changes over the Pacific/North American region. This feature will be discussed later. Also note that the PBL cooling over the core region is too strong in GEN. This reflects the unrealistic lag response in Tahiti Psl discussed already.

It is likely that the direct sources for the zonally symmetric warming are the release of latent heat due to condensation and the vertical transport of surface energy by the enhanced moist convection. Barnett et al. (1991) have clearly demonstrated that the forcing in the free troposphere is caused by condensational heating while the direct role of local air-sea heat exchange is negligible. Some evidence supports the notion that the energy originates at the surface, is transported upward in the core region, and then spreads throughout the tropical free troposphere (Angell and Korshover 1983; Pan and Oort 1983; Barnett 1985). This argument is reinforced by the recent results of Gutzler (1996), who found that, during 1970–1994, the observed mid- and upper-tropospheric temperatures over the tropical west Pacific are not associated with local SST. Rather, they are significantly correlated with SST in the central and east Pacific.

The exact mechanism that causes this spread of heat, however, is not known. Scaling arguments show that, for planetary scale time-averaged flow in low latitudes, the large heating observed in convective regions must be balanced by vertical advection. The dominance of zonal winds therein implies insignificant eddy meridional transport. Thus, the heat and momentum are transferred primarily by axisymmetric motions in the tropics. Barnett et al. (1991) argued that, during the warm stage of ENSO, the tropospheric monopole is essentially caused by anomalous condensational heating in deep convective clouds, which trigger stronger subsidence and adiabatic warming over an unusually large region of the tropics. The opposite conditions hold for a cold event. In addition, equatorial Kelvin waves, which are non-dispersive and eastward propagating, have a meridional scale of around 2000 km. These trapped disturbances may also play an important

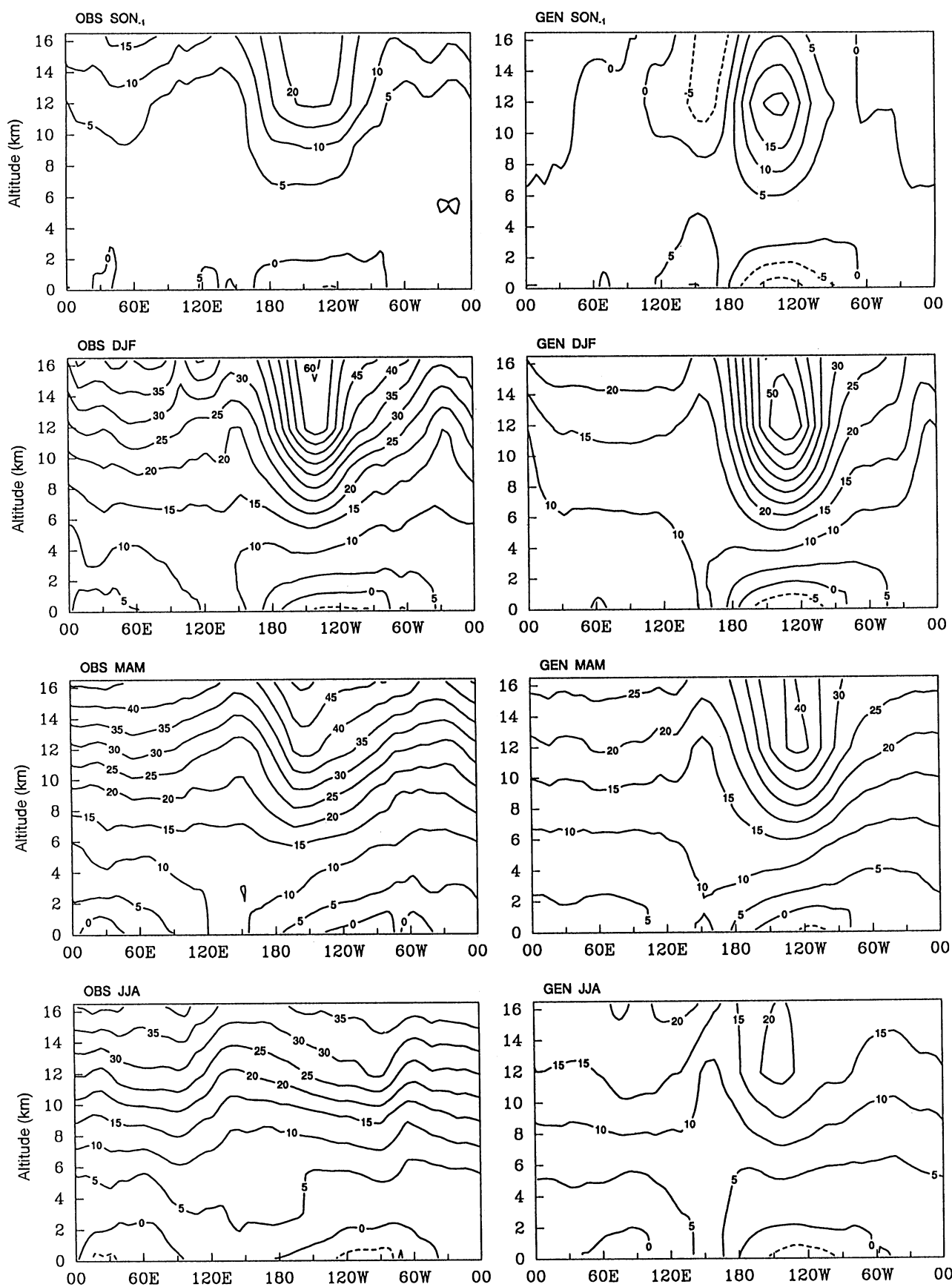


**Fig. 10.** Seasonal longitude-altitude geopotential height anomaly composites, identified with the warm stage of ENSO (see text) and averaged over the equatorial belt ( $5^{\circ}\text{S}$ – $5^{\circ}\text{N}$ ). The contour interval is 5 m, where *negative values are dashed*. The labels *SON<sub>-1</sub>*, *DJF*, *MAM*, *JJA* denote the consecutive seasons of autumn, winter, spring and summer

role in the tropical atmospheric response to highly localized thermal forcings. But the concise link between Kelvin wave activity and the spread of equatorial heating has not been established.

5.3 Equatorial anomaly longitudinal variations

During the typical ENSO life cycle, tropical Pacific SST anomaly signs tend to change in the vicinity of the date line. These anomalies signify either the abnormal eastward expansion of warm waters from the west Pacific or the westward intrusion of the cold tongue from the South American coast. As a result, interannual SST variability in

the tropics is most vigorous over the central and east Pacific. Atmospheric circulation responses to these SST variations are expected to have unique longitudinal characteristics. This is depicted in Fig. 11 by the Hovmöller diagram of 5°S–5°N averaged OLR. Information is displayed between 100°E and 90°W, where realistic signals in both GCMs are identified by the  $R_{oe}$  analysis (Fig. 6). There are two notable features.

1. The eastward propagation of the signal is clearly shown in both the observed and simulated OLR fields. Three ENSO life cycles can be distinguished, with transitions that occur approximately during summer in 1983 and 1988. Each cycle is identified with a dominant

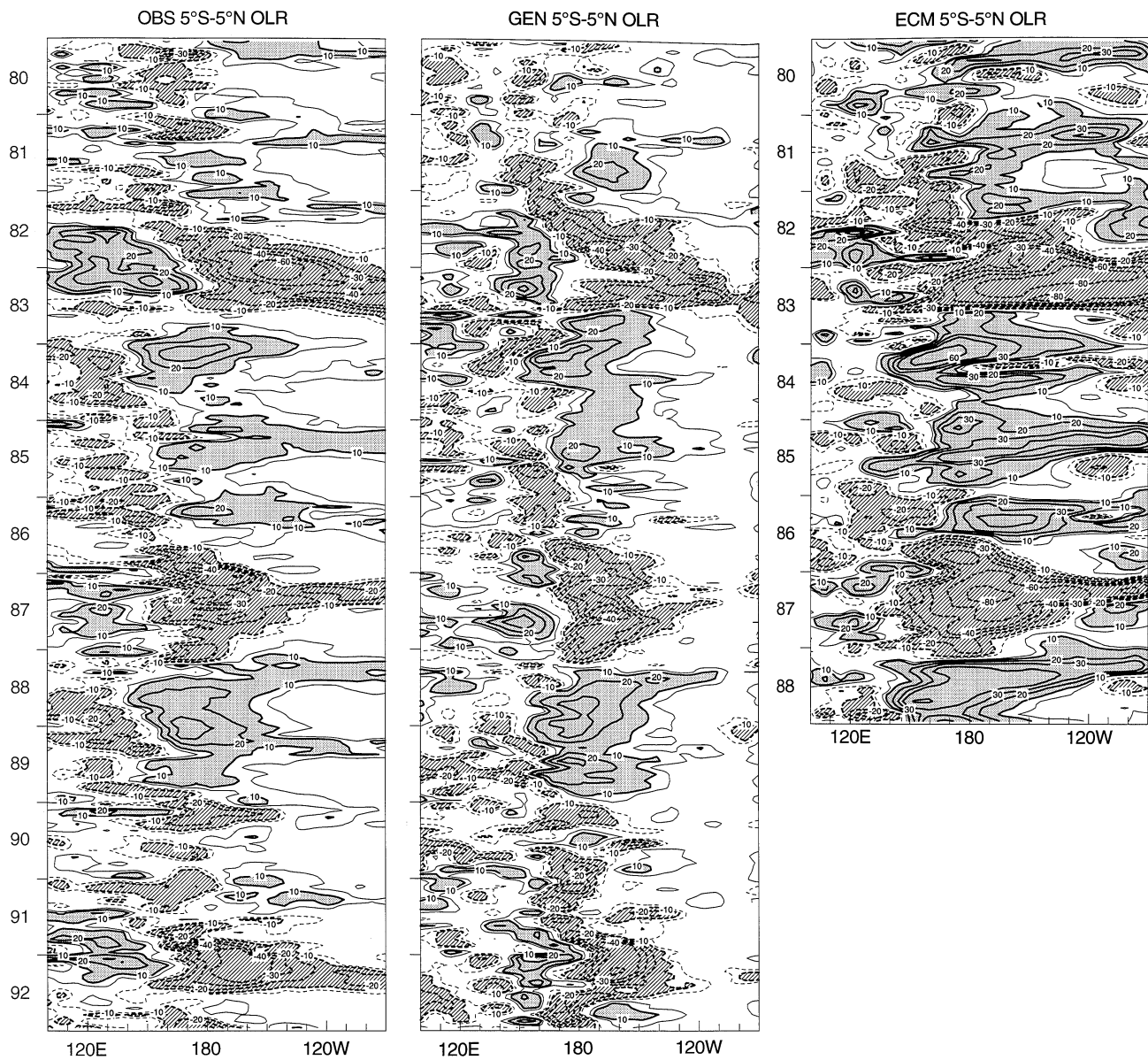


**Fig. 11.** Hovmöller diagrams of 5°S–5°N averaged monthly OLR anomalies. The *abscissas* represent longitude while the *ordinates* denote calendar month from January 1980 (*top*) to December 1992 (*bottom*). The contours are 5 (*thin*), 10, 20, 30, 40, 60 and 80  $\text{Wm}^{-2}$ ,

where *negative* values are *dashed*. The *shaded* and *hatched* areas indicate positive and negative anomaly magnitudes larger than one standard deviation. Anomalies and deviations are based on the 1980–1988 monthly climatology



east-west dipole structure. During the cold phase, a negative anomaly (enhanced convection) first appears in the west Pacific, with its opposite pole located to the east. The dipole gradually moves to the east such that the initial polarity is reversed during El Niño onset. Over the next year or so, the negative anomaly overspreads the central and east-central Pacific while the positive pole covers the west Pacific. The anomaly then weakens and, after a quick transition, the dipole polarity reverses and a new cycle begins. Note that the anomalous SST gradients (Laplacian) initiate PBL wind convergence which, in turn, determines the occurrence of deep convection (Barnett et al. 1991). The ascending branch of the zonal Walker circulation, intense precipitation and high/cold cloud tops are each associated with the convection. Thus, the successful simulation of OLR evolution implies that both models capture the essential links between SST, the circulation and convection over the Pacific.

2. When compared with observations, the east-west expansion of the GEN OLR anomaly in the central Pacific is too small. As a result, the western pole of the zonal dipole pattern is confined to the east of observations. In contrast, as shown in Fig. 9, the ECM anomaly magnitudes are greatly overestimated and coverage is more extensive than observations. Although the ECM anomaly amplitude is inflated, there is greater overlap with observations and, as indicated by the  $R_{oe}$  analysis, ECM (relative to GEN) produces a larger area with realistic OLR signals.

#### 5.4 Tropical-extratropical interactions

It is clear that the most realistic simulation of tropical-extratropical interactions occurs over the central/east Pacific (Fig. 6). The evolution of circulation anomalies in this region is illustrated by Hovmöller diagrams of OLR averaged between  $160^{\circ}\text{E}$ – $140^{\circ}\text{W}$  and  $U_{200}$  between  $160^{\circ}\text{E}$ – $100^{\circ}\text{W}$  (Fig. 12). These regional specifications are determined by the  $R_{oe}$  analysis (Fig. 6) and confirmed by the equatorial evolution (Fig. 11). There are three major features in Fig. 12.

1. The two indices are positively correlated in the tropics. Parallel to the equatorial anomaly centers are subtropical centers of opposite sign, where the OLR centers are located between the  $U_{200}$  dipoles. This supports the fact that, during warm episodes, two anticyclonic gyres straddle the equator while the meridional Hadley circulations strengthen. Near the equator, anomalous upper-level easterly and lower-level westerly winds are identified with ascending motions and enhanced rainfall. In the subtropics descending motions and decreased precipitation occur where, on the poleward margins, the anticyclones produce westerly wind anomalies that cause the upper-level subtropical jets to intensify. The circulation anomalies are reversed during cold phases. Bjerknes (1969) argued that anticyclonic (cyclonic) responses occur because the stronger (weaker) Hadley circulations increase (decrease) the poleward transport of angular momentum in the upper troposphere. Both GCMs simulate these relationships.

2. Subtropical  $U_{200}$  responses are relatively insensitive to the precise location of heating anomalies in the tropical Pacific. The OLR plots show that heating anomalies propagate to the east along the equator (Fig. 11) and move to the south over the central Pacific (Fig. 12). The latitudinal locations of wind anomalies, however, remain approximately the same and are centered near  $30^{\circ}\text{S}$  and  $30^{\circ}\text{N}$ . Both GCMs reproduce this feature. We will elaborate this point in Sect. 6.

3. In both the tropics and subtropics, the ECM OLR anomaly magnitudes are systematically overestimated, whereas the GEN values are slightly smaller than observations. In contrast, the simulated wind anomaly amplitudes are generally realistic.

It is important to note that little predictability in wind and convection is found over the Eurasian sector, including the Indian Ocean and the tropical west Pacific. In addition to the aforementioned slower equatorial heat spread that results from the SST and convection anomalies over the tropical central/east Pacific, this failure may be caused by the unrealistic representation of the eastward progression of convection from the Indian Ocean to the west Pacific. Kiladis et al. (1994) and Meehl et al. (1996) have shown that, on the time scale of the Madden-Julian Oscillation (MJO; Madden and Julian 1994), convection over the Indian Ocean and the tropical west Pacific is linked by a downstream mid-latitude wave train. Thus, this eastward progression plays an important role in tropical-mid-latitude interactions. Most GCMs, however, are unable to realistically simulate the MJO (Slingo et al. 1996) and, hence, may produce incorrect responses to the SST forcing.

The results presented in this section indicate that the permutation significance evaluation procedure developed in Sect. 3 is a robust test that leads to the identification of physically meaningful signals. Higher ECM anomaly predictability is found to be associated with a more realistic basic climate state, especially in the zonal mean circulation. Greater OLR predictability, however, results from the compensating effects of realistic timing and systematically larger amplitudes in the temporal/spatial variability of ECM cloud-radiation interactions. Note that, as indicated by the OLR features, a more vigorous ECM hydrologic cycle is identified with stronger Hadley and Walker circulations. When compared with GEN, the ECM parametrizations for convection and cloud-radiative interactions are more sensitive to the tropical SST forcing. These can also enhance ECM extratropical signals and, hence, result in greater predictability of tropically forced signals (Meehl and Albrecht 1991; Kumar et al. 1996).

## 6 Extreme anomaly teleconnection

The  $R_{oe}$  analysis in Sect. 4 shows that the overall model predictability of SST anomaly forced circulation changes is confined to a relatively small fraction of the total area, mostly over the tropics and subtropics. This occurs because, in the extratropics, internal variability (as described by the sensitivity to initial states) dominates the forced

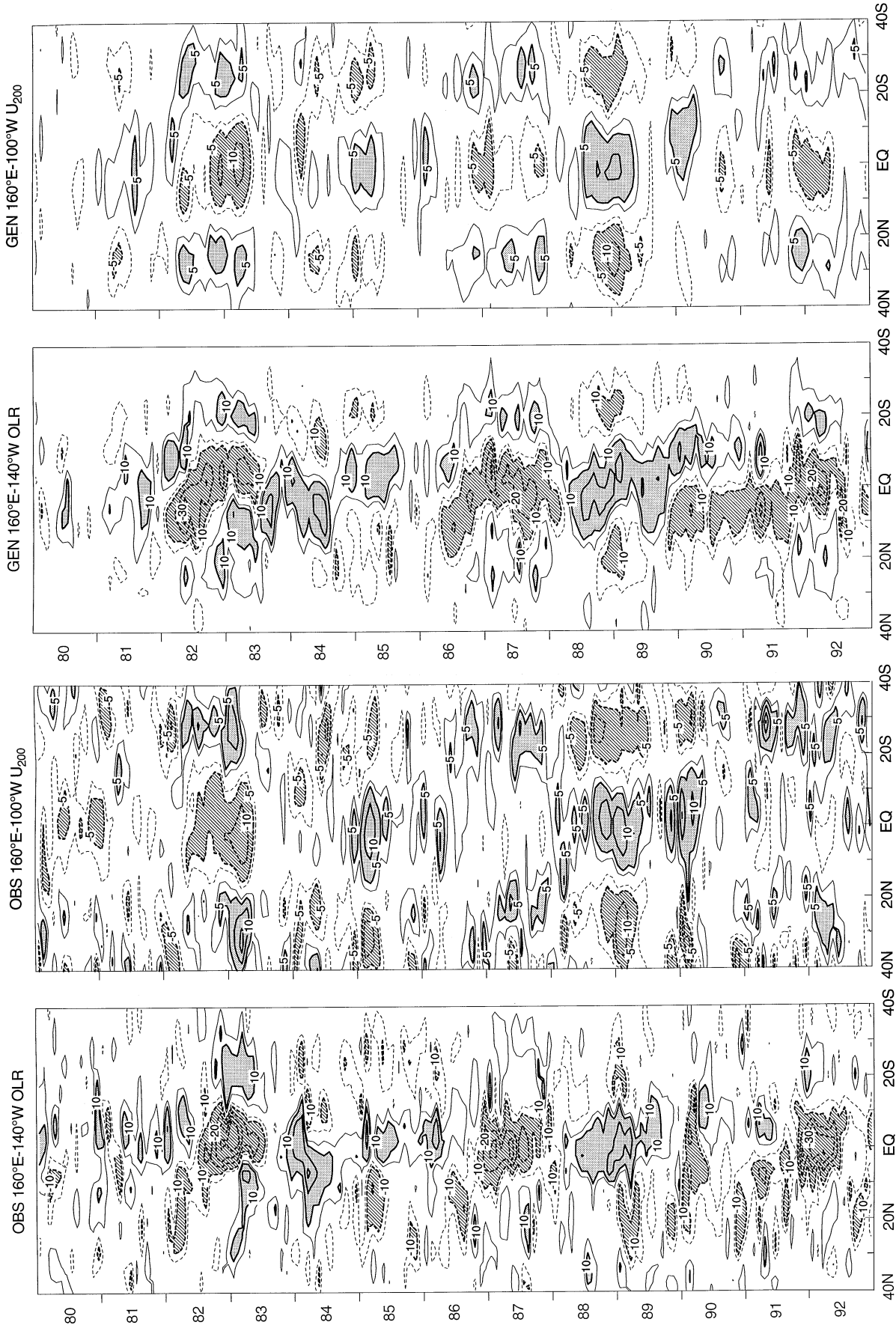


**Fig. 12.** Latitude-month Hovmöller diagrams of 160°E–140°W averaged OLR and 160°E–100°W mean  $U_{200}$  anomalies. The contours are 5 (thin), 10, 20, 30, 40, 60 and 80  $\text{W m}^{-2}$  for OLR and 2.5 (thin), 5, 10, 15, 20, 25  $\text{ms}^{-1}$  for  $U_{200}$ , where negative values are dashed. See Fig. 8 caption for all other information

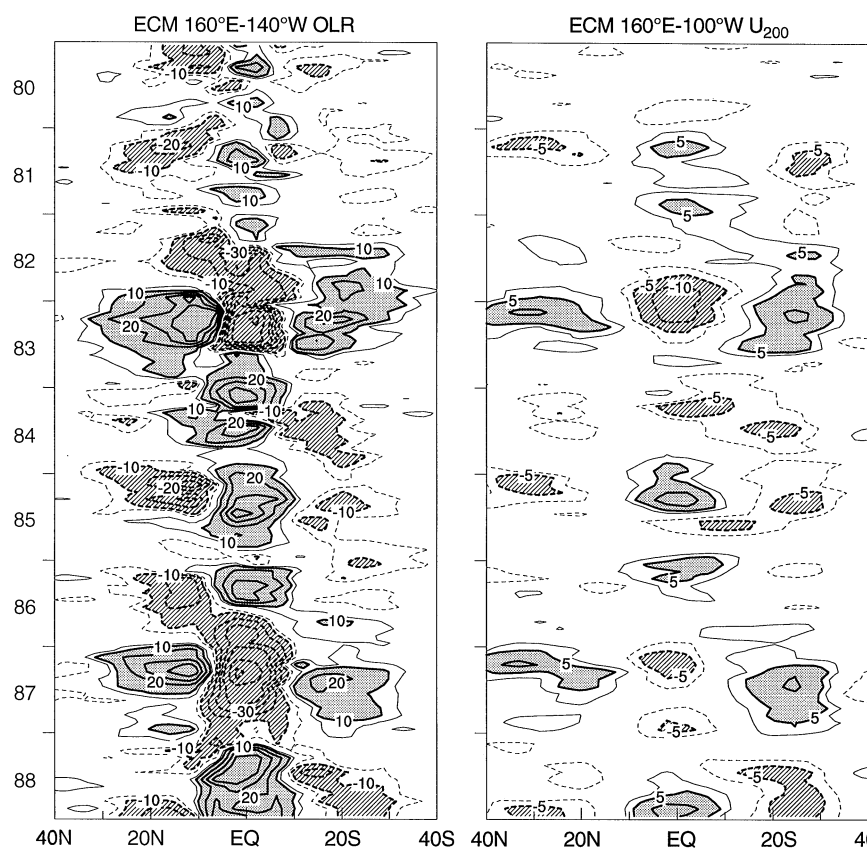


Fig. 12 (Continued)

signals. It can be argued that a broader region of robust and realistic signals can be identified during SST extreme anomaly periods. This section studies the predictability of extreme teleconnections when strong ENSO events are observed.

To provide an upper bound estimation of predictability, individual winter (DJF) averages for 1982/83, 1984/85, 1986/87, 1988/89 and 1991/92 are examined. These winters are expected to have most vigorous and extensive teleconnection signals. Model values represent the ensemble means of all runs with different initial states. To detect robust signals, the regions where local anomaly magnitudes are larger than one standard deviation are shown in both the observed and simulated fields. In addition, the areas with  $C_c$  values (defined in Sect. 3) greater than 0.5 are depicted to indicate anomalies that are significantly coherent between individual realizations. Note that anomalies and deviations are based on the 1980–1988 monthly climatology.

Figure 13 illustrates the  $U_{200}$ ,  $U_{850}$  and OLR fields for the 1982/83 extreme case. The other cases are not shown because their principal features are similar, especially over the Pacific Basin, although a few distinctions will be discussed. For convenience, the results are described in terms of positive SST anomalies in the central and east-central equatorial Pacific. Three outstanding features are identified.

1. Dominant signals are found mostly in the Pacific Basin. The models correctly simulate the enhanced

convection and rainfall over the tropical central Pacific. This indicates a realistic merging of rainbands identified with the Intertropical Convergence Zone, the South Pacific Convergence Zone and the west Pacific Convergence Zone. The anomalous equatorial easterlies and subtropical westerlies, which comprise the upper tropospheric anticyclone pair that straddles the equator, are located nearly adjacent to the enhanced convection. These anticyclonic gyres are a direct response to upper-level divergence over the convective region, which, due to the Earth's rotation produces anticyclonic vorticity along its poleward boundaries. As a result, the meridional Hadley circulations are intensified such that stronger subsidence and less rainfall (higher OLR) occur in the subtropics. Meanwhile the cyclonic anomalies seen at higher latitudes imply stronger meridional Ferrel cells. These anomalies form wave trains that link the tropics and extratropics. The Northern Hemisphere train appears in the  $H_{500}$  field (not shown) and is reminiscent of the Pacific/North American pattern (Wallace and Gutzler 1981). The centers of this pattern occur along a “great circle” arc and are widely believed to be generated through the Rossby wave dispersion mechanism. This feature can be reproduced by most GCMs with a variety of driving forces: forcing by equatorial rainfall anomalies is just one possibility (e.g., Liang et al. 1996).

Important differences between observations and simulations are also found over the Pacific Ocean. For example, in the tropics, GEN produces a smaller area of enhanced convection (decreased OLR) while ECM greatly

overestimates the anomaly magnitude, especially in the 1982/83 event. Although subtropical convection in both models is suppressed, the GEN OLR anomalies appear to be realistic while ECM values are too large. The three anomaly center locations, however, are realistic in both models. Over the far west Pacific, the suppression of convection is much smaller in both models than observations. Model failure to represent convective activity leads to errors in other fields (see below).

Significant anomaly signatures are identified over additional specific regions, but the agreement between observations and simulations is much less obvious than that over the Pacific Basin. For example, observed convection is generally suppressed over Brazil and the equatorial Atlantic, while it is enhanced in the subtropics of both hemispheres. This OLR feature and the associated  $U_{200}$  anomaly pattern (equatorial westerlies and subtropical easterlies) are, in essence, reproduced by ECM, while the

GEN signal is much weaker. This model contrast is clearly indicated by the  $R_{oe}$  pattern in Fig. 6. Enhanced convection is repeatedly observed over the Indian Ocean during 1982/83 and 1991/92 while it is suppressed at the same time over the far west Pacific. This pattern is accompanied by large positive  $U_{200}$  anomalies over south Asia/Australia and negative values along the polarward sides, both of which merge into a northeast wave train. Similar responses are generated only by ECM. Over west Eurasia and Africa, a meridional wave train of  $U_{200}$  anomalies is observed and simulated in both models. The magnitude and/or location of simulated anomalies, however, disagrees with observations.

2. Given that the longitudinal location of enhanced tropical convection changes from year to year, the  $U_{200}$  anomaly center locations over the Pacific are essentially constant in observations while they vary in both models. Stronger (Lweaker) convection is observed

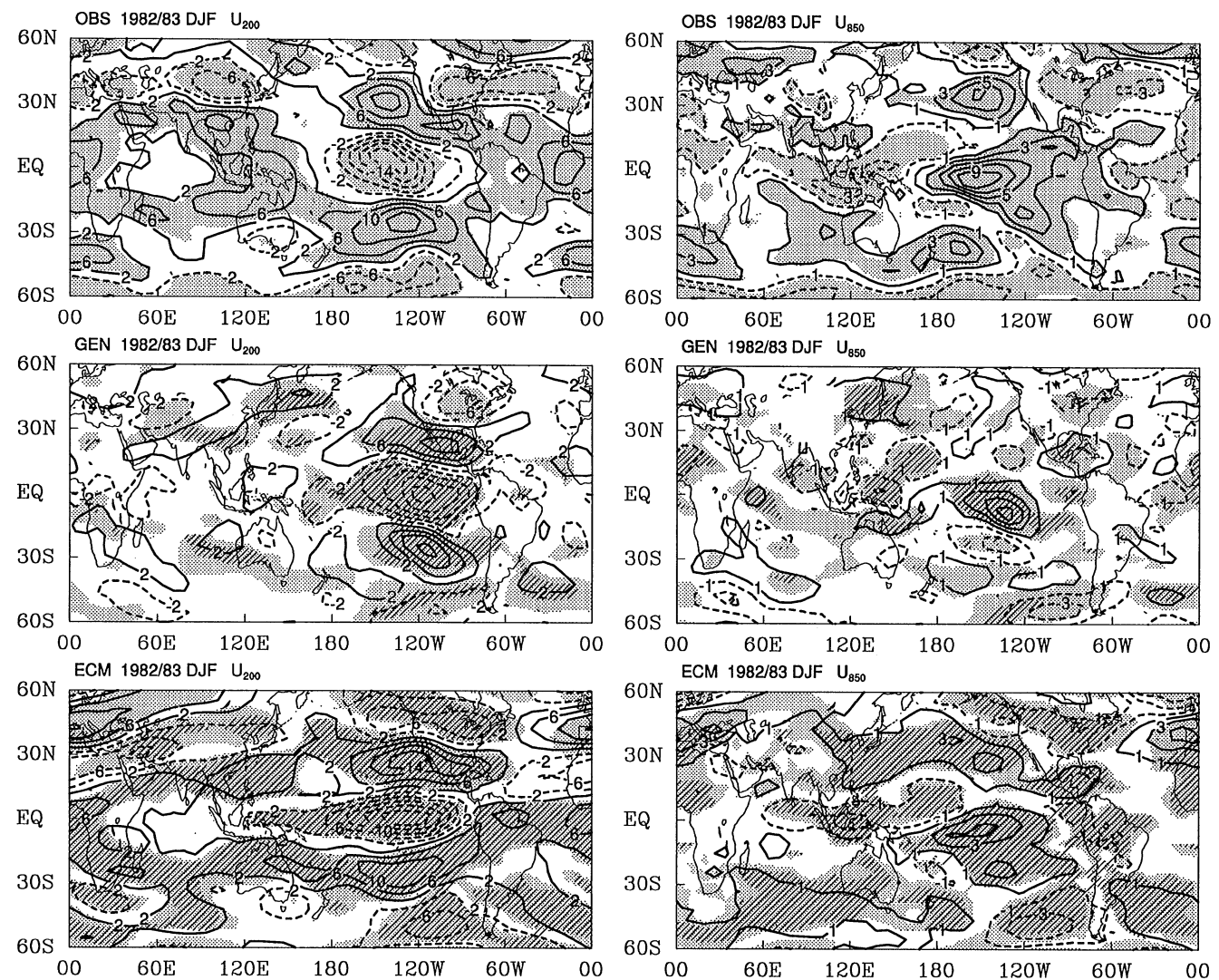


**Fig. 13.** Extreme 1982/83 winter (DJF)  $U_{200}$ ,  $U_{850}$  and OLR anomaly distributions. The contour intervals/reference contours are  $4/2\text{ ms}^{-1}$  for  $U_{200}$ ,  $2/1\text{ ms}^{-1}$  for  $U_{850}$ , and  $10/5\text{ Wm}^{-2}$  for OLR.

The shaded areas indicate local anomaly magnitudes larger than one standard deviation, while the hatched areas denote  $C_e$  values larger than 0.5

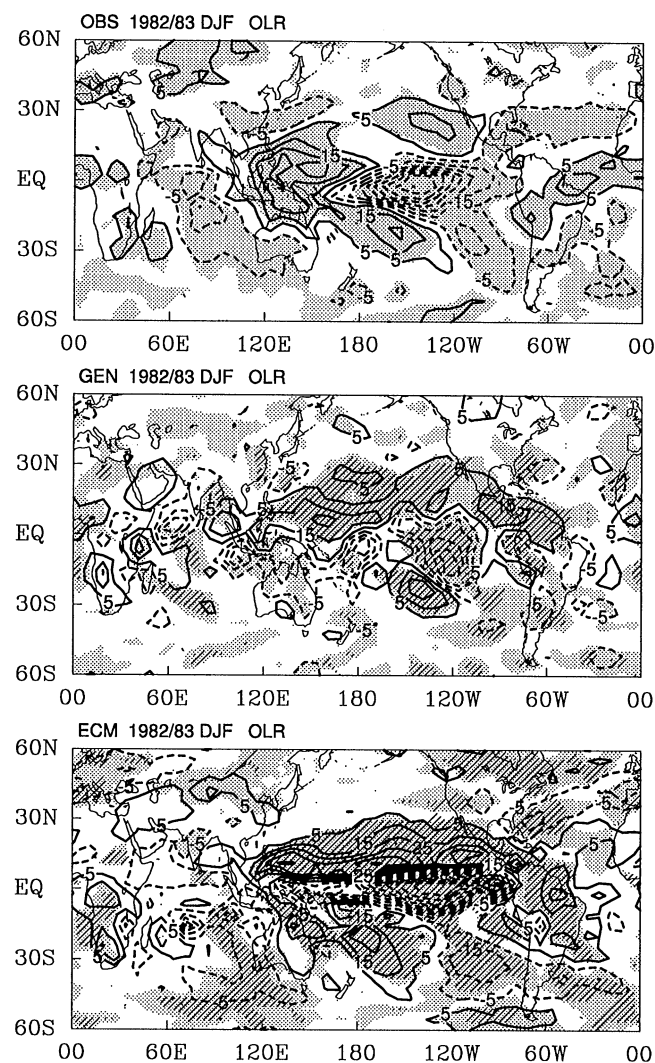


Fig. 13. (Continued)

along the data line during (1984/85), 1986/87, (1988/89) and 1991/92, whereas it is centered near  $140^{\circ}\text{W}$  in 1982/83. Both models correctly simulate the convection center locations, except the GEN 1982/83 center shifts  $20^{\circ}$  to the east of observations. For all cases, observed  $U_{200}$  anomaly centers are aligned along  $140^{\circ}\text{W}$ . In contrast, ECM 1982/83, GEN 1982/83 and 1991/92  $U_{200}$  anomalies are found at  $120^{\circ}\text{W}$ . Recall that, as with observations, the  $U_{200}$  anomaly latitudinal locations are generally stationary (see Sect. 5).

Sardeshmukh and Hoskins (1988) showed that, during winter, when strong stationary waves occur, the Northern Hemisphere extratropical response takes the form of a geographically fixed normal-mode that is insensitive to the precise location of the tropical rainfall anomaly forcing. They argued that, for heating embedded in the equatorial easterlies, the effective Rossby wave source in the context of a barotropic model lies mainly near the subtropical westerly jets, and its intensity depends on jet strength and sharpness. This source is nearly antisymmetric about the equator and its subtropical component is

relatively independent of the equatorial heating position in the west or central Pacific. This theory may partially explain why observed  $U_{200}$  anomaly positions remain unchanged.

What matters then is why both models fail to produce  $U_{200}$  response centers at a fixed longitude. The reasons are not fully understood. One possibility is related to model biases in the basic flow. Ting and Sardeshmukh (1993) investigated the steady linear response of a baroclinic atmosphere to an equatorial diabatic heating source at various longitudes. The response is characterized by a wave train that arches to the northeast from the west tropical Pacific Ocean and a quadrupole structure in the vicinity of the heating. (A similar feature is seen in our 1982/83 observed  $U_{200}$  plot). The wave train takes the form of normal modes while the quadrupole moves with the heating across the Pacific. When the source is imposed on the ECMWF analysis observed basic state, the normal-mode characteristics extend into the deep tropics, whereas the moving quadrupole is apparent only in the Southern Hemisphere. In contrast, when slightly biased GCM basic flow is used, the quadrupole dominates the tropics and subtropics.

3. One serious problem in both models is the erroneous relationship between upper and lower tropospheric wind responses, which indicates unrealistic mechanisms associated with the generation and distribution of momentum. To highlight this issue, we focus on the Pacific Basin. In the 1982/83 event, both models realistically simulate  $U_{200}$  anomaly characteristics in the east-central Pacific, although the location is systematically shifted  $20^{\circ}$  to the east. In addition, substantial  $U_{850}$  responses are observed: a vigorous westerly center is identified over a broad region that extends from the central equatorial to east tropical/subtropical Pacific. Strong westerly centers also occur along  $140^{\circ}\text{W}$  at both  $30^{\circ}\text{S}$  and  $30^{\circ}\text{N}$ . This structure causes a baroclinic response to occur over the enhanced convection region in the central equatorial Pacific, whereas barotropic responses dominate the east and extratropical Pacific. GEN generates a slightly weaker westerly  $U_{850}$  anomaly that is confined to the central equatorial Pacific, while the responses elsewhere are smaller or of the opposite sign. In spite of a realistic spatial pattern, ECM systematically underestimates  $U_{850}$  anomaly magnitudes (less than half of observations).

Although biases differ from case to case, the simulated vertical wind structure, without exception, is unrealistic.  $U_{850}$  westerly anomaly coverage is associated with the areal extension of enhanced tropical convection. As discussed earlier, anomalous SST gradients determine the initial PBL wind while the vertical mass and moisture flux through the PBL top establishes the convective heating principal location. For this reason, in the 1982/83 case, the negative OLR anomaly in GEN covers a small area and is identified with a highly localized  $U_{850}$  westerly center over the central equatorial Pacific. In contrast, the coverage of both anomalies in ECM is much more realistic. This result can be generalized to other cases. A critical question is why the wind response spatial structure in both models is poorly defined. There is no obvious answer at this time. Nevertheless, some speculation is presented next.

In the 1982/83 event, the model vertical wind shear anomaly over the central equatorial Pacific is too weak. This may result from the lack of upgradient momentum transport by intense convection. Although both models include vertical momentum transport via convective mixing, this process can only redistribute momentum in the direction that reduces vertical shear (i.e., downgradient transport). Observational and theoretical studies have shown that upgradient transport, which actually increases vertical shear, can also occur (e.g., Wu and Yanai 1994). If this were the case the  $U_{850}$  westerly anomaly would be more intense (or extensive) and the  $U_{200}$  easterly anomaly larger. Since the  $U_{200}$  anomalies are sufficiently large, the enhanced tropical easterly momentum must be transferred through the Hadley circulation first poleward then downward into the lower levels such that realistic subtropical westerly anomalies could be obtained. The mechanism for this transfer process is not known.

An additional cause is the existence of model biases in the basic flow (Figs. 1–2). It is known that extratropical responses forced by the equatorial rainfall anomaly are very sensitive to changes in the basic state (Sardeshmukh and Hoskins 1988; Ting and Sardeshmukh 1993). A small shift in the subtropical jet can produce substantial changes in topographically forced stationary waves (da Silva and Lindzen 1993) and, hence, result in a false interaction with the tropical circulation. Furthermore, as discussed in Sect. 5, the inefficient vertical and horizontal transport of enhanced convection thermal forcing may partially explain the lack of realistic responses in GEN over regions other than the Pacific Basin.

There are two caveats that may affect our comparisons. First, as noted in Sect. 2, breaks occur in the observed data record. This introduces uncertainties to signal identification that cannot be resolved until the improved re-analysis data are available. Second, horizontal resolutions differ. The coarse GEN resolution may be responsible for serious basic flow biases (Liang et al. 1995a) and, thus, result in the low predictability of SST forced climate responses.

As a final remark, a successful PBL wind anomaly simulation is required to produce a realistic ENSO prediction when the atmospheric GCM is coupled with a full dynamic ocean. This is because surface wind stress is a key factor involved with interactive processes in the coupled system. For example, in the tropics, the SST is not only affected by heat exchange, but much of its variability arises from dynamical adjustments to surface wind stress (e.g., Palmer and Anderson 1994). The PBL wind anomaly underestimation identified in this study is common to other GCMs and, consequently, a major obstacle in the coupling practice.

## 7 Summary and conclusions

The predictability of atmospheric responses to global SST anomalies is evaluated using the ensemble simulations of two GCMs: the GENESIS version 1.5 (GEN) and the ECMWF cycle 36 (ECM). These integrations incorporate observed SST variations but start from different initial land and atmospheric states. Five GEN 1980–1992 and six ECM 1980–1988 realizations are compared with ob-

servations to distinguish predictable SST forced climate signals from internal variability and to study predictability dependence on the model basic climatology.

To compare a single observed realization with multiple simulations, correlation analysis and significance evaluation techniques are developed on the basis of permutations. The rationale behind the use of this permutation method is that sea surface conditions in all model runs are forced to vary in transient with observations and, thus, robust climate responses to this forcing must be manifested in instantaneous correlations between independent realizations. A correlation probability distribution is then constructed using 1000 permutations where the sequence of any original time series is re-ordered in random without replication. For each climate variable and grid point, a significance threshold is determined from this distribution such that 90% of permutations have smaller correlation coefficients. Note that the ensemble mean instantaneous correlation is based on all distinct combinations between observed and/or simulated realizations. In addition, when extreme anomalies (with magnitudes larger than one standard deviation) are compared, a coherent correlation measure is designed to identify consistency between individual realizations.

These techniques are first applied to identify signal regions where realistic responses are simulated. The evolutionary responses of each model atmosphere over these regions are then examined using the time series of selected circulation indices as well as zonal and meridional Hovmöller diagrams. This analysis demonstrates that the developed techniques can determine physically meaningful climate signals forced by SST anomalies from internal model variability. Finally, we study the predictability of anomaly teleconnections when extreme ENSO events are observed. Such predictability represents the upper limit of GCM capability to reproduce observed climate changes in response to SST anomalies. Five variables are chosen to represent the atmospheric circulation: outgoing longwave radiation (OLR), 200/850 hPa zonal wind ( $U_{200}/U_{850}$ ), 500 hPa height ( $H_{500}$ ) and sea-level pressure (Psl). These analyses lead to the following findings:

1. Internal variability is dominant for all variables while robust model responses, which are independent of initial condition, account for a small fraction of the globe. When annually averaged, this fraction, which is variable dependent, ranges from 5.2 to 25.0% in GEN and 16.1 to 38.1% for ECM. Due to the existence of model biases, only a portion of the robust responses is realistic. The areas of realistic  $U_{850}$ , OLR,  $U_{200}$ , Psl,  $H_{500}$  signals are, respectively, 3.1, 5.0, 7.9, 8.1, 19.8% in GEN and 6.3, 8.4, 11.2, 13.7, 28.0% in ECM. More than 95% of these signal areas occur between 35°S–35°N. Clearly, relative to GEN, ECM exhibits less sensitivity to initial conditions and a higher predictability of SST forced climate changes. Note that, in the order of the listed variables, sensitivity decreases while predictability increases.

2. The overall predictable signals are concentrated in the tropical and subtropical Pacific, and are identified with typical ENSO phenomena that occur in response to

SST and diabatic heating anomalies over the central equatorial Pacific. During warm episodes, the equatorial zonal Walker circulation moves eastward and causes enhanced (suppressed) convection over the central (far west) Pacific while the meridional Hadley circulation in the central/east Pacific intensifies such that two anticyclonic gyres straddle the equator with anomalous equatorial easterlies and subtropical westerlies in the upper troposphere. The free troposphere experiences a systematic warming throughout the entire tropical belt. The near surface east-west pressure gradient decreases, where Psl falls in the southeast tropical Pacific and rises over the Indo/Australian region. Finally, the extratropical teleconnection is dominant over the northern Pacific/North American region. The circulation anomaly signs are reversed during cold phases.

3. For GEN during warm ENSO events, the convection does not carry lower level energy to a sufficiently high altitude. In addition, the spread of the tropospheric warming along the equator is much slower and the anomaly magnitude smaller than observations. Thus, the warming magnitude in the tropics, away from the enhanced convection region, is substantially underestimated. As a consequence, observed wind and associated circulation changes over Eurasia, Africa, the west Pacific and Indian Oceans are poorly simulated. Similar ECM errors exist in these regions and may also be attributed to unrealistic energy transport. This final point needs to be verified when corresponding ECM data are available.

4. Realistic  $U_{200}$  responses in both GCMs are found in the central/east Pacific and take the form of meridional wave trains that emanate from the equator to the extratropics in both hemispheres. Much less predictability is identified with  $U_{850}$ . For example, during the 1982/83 El Niño, a vigorous westerly anomaly is observed over a broad region that extends from the central equatorial to east tropical/subtropical Pacific Ocean while strong westerly centers along  $140^{\circ}\text{W}$  occur simultaneously near  $30^{\circ}\text{S}$  and  $30^{\circ}\text{N}$ . GEN simulates a slightly weaker westerly anomaly that is confined to the central equatorial Pacific while the response elsewhere is diminished. In contrast, ECM systematically underestimates anomaly magnitude, although the spatial pattern is more realistic. The erroneous near surface wind (and hence surface stress) responses will result in an unrealistic air-sea interaction that ultimately leads to a poor prediction when the atmospheric GCM is fully coupled with a dynamic ocean model. We speculate that the incorporation of upgradient momentum transport into the convection parametrization will reduce this errors.

5. ECM achieves higher predictive skill than GEN, not only in the Pacific Basin but also over the Atlantic. This results from (a) a more realistic basic climatology, especially of the upper-level wind circulation, that produces more realistic interactions between the mean flow, stationary waves and tropical forcing; (b) a more vigorous hydrologic cycle that amplifies the tropical forcing signals, which can exceed internal variability and be more efficiently transported from the forcing region.

Note that breaks in the observed data record may have a minor impact on our comparison results. This can be

minimized by using the newly available re-analysis data. Resolution difference may also contribute to model predictability contrast and, thus, warrant future investigation. In addition, because all other available AMIP simulations are for a single realization (Gates 1992), our research is based on only two GCMs. The universality of our findings requires further studies with ensemble runs for other GCMs. Nevertheless, the overall results indicate that GCM configuration improvements, such as the convective heat and momentum transport parametrization and basic climate (especially the wind circulation) representation, could substantially increase predictive skill. Ultimately, the atmospheric GCM generates internal variability (as measured by sensitivity to initial condition) that is equivalent to observed natural variability and, therefore, achieves the potential predictability when a perfect forecast of SST variations is achieved.

*Acknowledgements.* We thank K.E. Trenberth for the availability of the ECMWF analysis, R.W. Reynolds for providing the NOAA blended SST analysis and J.E. Janowiak for the NOAA OLR data. We also thank J.D. Horel for helpful discussion and references on the tropical zonal symmetric response. The study was supported by grants from the Environmental Sciences Research Division of the Department of Energy and the Climate Dynamics Section of the National Science Foundation. K.R. Sperber was supported under the auspices of the US Department of Energy Environmental Sciences Division at the Lawrence Livermore National Laboratory under contract W-7405-ENG-48.

## References

- Angell JK, Korshover J (1983) Global temperature variations in the troposphere and stratosphere, 1958–1982. *Mon Weather Rev* 111: 901–921
- Barnett TP (1985) Three-dimensional structure of low-frequency pressure variations in the tropical atmosphere. *J Atmos Sci* 42: 2798–2803
- Barnett TP, Latif M, Eirk E, Roeckner E (1991) On ENSO physics. *J Clim* 4: 487–515
- Barnett TP, Latif M, Graham N, Flügel M, Pazan S, White W (1993) ENSO and ENSO-related predictability, Part I: prediction of equatorial Pacific sea surface temperature with a hybrid coupled ocean-atmosphere model. *J Clim* 8: 1545–1566
- Barnett TP, Bengtsson L, Arpe K, Flügel M, Graham N, Latif M, Ritchie J, Roeckner E, Schlese U, Schulzweida U, Tyree M (1994) Forecasting global ENSO-related climate anomalies. *Tellus* 46A: 381–397
- Barnston AG, van den Dool HM, Zebiak SE, Barnett TP, Ji M, Rodenhuis DR, Cane MA, Leetmaa A, Graham NE, Ropelewski CR, Kousky VE, O'Lenic EA, Livezey RE (1994) Long-lead seasonal forecasts – Where do we stand? *Bull Am Meteorol Soc* 75: 2097–2114
- Bengtsson L, Schlese U, Roeckner E, Latif M, Barnett TP, Graham N (1993) A two-tiered approach to long-range climate forecasting. *Science* 261: 1026–1029
- Bjerknes J (1969) Atmospheric teleconnections from the equatorial Pacific. *Mon Weather Rev* 97: 163–172
- Boer GJ, Arpe K, Blackburn M, D'Arrigo M, Gates WL, Hart TL, le Treut H, Roeckner E, Sheinin DA, Simmonds I, Smith RNB, Tokioka T, Wetherald RT, Williamson D (1992) Some results from an intercomparison of the climates simulated by 14 atmospheric general circulation models. *J Geophys Res* 97: 12771–12786
- Chervin RM (1986) Interannual variability and seasonal climate predictability. *J Atmos Sci* 43: 233–251



- de Silva AM, Lindzen RS (1993) On the establishment of stationary waves in the Northern Hemisphere winter. *J Atmos Sci* 50: 43–61
- Fennessy MJ, Shukla J (1991) Comparison of the impact of the 1982/83 and 1986/87 Pacific SST anomalies on time-mean predictions of atmospheric circulation. *J Clim* 4: 407–423
- Gates WL (1992) AMIP: The Atmospheric Model Inter-comparison Project. *Bull Am Meteorol Soc* 73: 1962–1970
- Geisler JE, Blackmon ML, Bates GT, Munoz S (1985) Sensitivity of January climate response to the magnitude and position of equatorial Pacific sea surface temperature anomalies. *J Atmos Sci* 42: 1037–1049
- Graham NE, Barnett TP (1995) ENSO and ENSO-related predictability, Part II: Northern Hemisphere 700-mb height prediction based on a hybrid coupled ENSO model. *J Clim* 8: 544–549
- Graham NE, Barnett TP, Wilde R, Ponater M, Schubert S (1994) On the roles of tropical and midlatitude SSTs in forcing interannual to interdecadal variability in the winter Northern Hemisphere circulation. *J Clim* 7: 1416–1441
- Gruber A, Krueger AF (1984) The status of the NOAA outgoing longwave radiation data set. *Bull Am Meteorol Soc* 65: 958–962
- Gutzler DS (1996) Low-frequency ocean-atmosphere variability across the tropical western Pacific. *J Atmos Sci* 53: 2773–2785
- Harzallah A, Sadourny R (1994) Internal versus SST-forced atmospheric variability as simulated by an atmospheric general circulation model. *J Clim* 8: 474–495
- Hoerling MP, Ting M (1994) Organization of extratropical transients during El Niño. *J Clim* 7: 745–766
- Horel JD, Wallace JM (1981) Planetary-scale atmospheric phenomena associated with the Southern Oscillation. *Mon Weather Rev* 109: 813–829
- Ji M, Kumar A, Leetmaa A (1994) An experimental coupled forecast system at the National Meteorological Center: some early results. *Tellus* 46A: 398–418
- Kiladis GN, Meehl GA, Weickmann KM (1994) Large-scale circulation associated with westerly wind bursts and deep convection over the western equatorial Pacific. *J Geophys Res* 99: 18527–18544
- Kumar A, Hoerling M, Ji M, Leetmaa A, Sardeshmukh P (1996) Assessing a GCM's suitability for making seasonal predictions. *J Clim* 9: 115–129
- Latif M, Sterl A, Maier-Reimer E, Junge MM (1993) Structure and predictability of the El Niño/Southern Oscillation phenomenon in a coupled ocean-atmosphere general circulation model. *J Clim* 6: 700–708
- Lau NC (1985) Modeling the seasonal dependence of the atmospheric response to observed El Niños in 1962–76. *Mon Weather Rev* 113: 1970–1996
- Lau NC, Nath MJ (1994) A modeling study of the relative roles of tropical and extratropical SST anomalies in the variability of the global atmosphere-ocean system. *J Clim* 7: 1184–1207
- Legates DR, Wilmott CJ (1990) Mean seasonal and spatial variability in gauge-corrected, global precipitation. *Int J Climatol* 10: 111–128
- Liang X-Z, Wang W-C (1995) A GCM study of the climatic effect of 1979–1992 ozone trend. In: Wang W-C, Isaksen ISA (eds) *Atmospheric ozone as a climate gas*, NATO ASI Series. pp 259–288
- Liang X-Z, Wang W-C, Samel AN, Pollard D, Thompson SL (1995a) Systematic biases of SUNYA/NCAR AMIP simulations. In: *Proc First Int AMIP Scientific Conference*, WCRP-92, WMO/TD-No 732, pp 181–186
- Liang X-Z, Wang W-C, Dudek MP (1995b) Interannual variability of regional climate and its change due to the greenhouse effect. *Global Planet Change* 10: 217–238
- Liang X-Z, Wang W-C, Dudek MP (1996) Northern hemispheric interannual teleconnection patterns and their changes due to the greenhouse effect. *J Clim* 9: 465–479
- Livezey RE, Chen WY (1983) Statistical field significance and its determination by Monte Carlo techniques. *Mon Weather Rev* 111: 46–59
- Madden RA (1976) Estimates of the natural variability of time-averaged sea-level pressure. *Mon Weather Rev* 104: 942–952
- Madden RA, Julian PR (1994) Observations of the 40–50-day tropical oscillation-A review. *Mon Weather Rev* 122: 814–837
- Meehl GA, Albrecht BA (1991) Response of a GCM with a hybrid convection scheme to a tropical Pacific sea surface temperature anomaly. *J Clim* 4: 672–688
- Meehl GA, Kiladis GN, Weickmann KM, Wheeler M, Gutzler DS, Compo GP (1996) Modulation of equatorial subseasonal convective episodes by tropical-extratropical interaction in the Indian and Pacific Ocean regions. *J Geophys Res* 101: 15033–15049
- Miyakoda K, Rosati A, Gudgel R (1993) Toward the GCM El Niño simulation. In: Shukla (ed) *Prediction of Interannual Climate Variations*, NATO ASI Series I: Global Environmental Change, vol 6, Springer, New York, Berlin, Heidelberg, pp 125–151
- Morcrette J-J (1990) Impact of changes to the radiation transfer parametrizations plus cloud optical properties in the ECMWF model. *Mon Weather Rev* 118: 847–873
- Morcrett J-J (1991) Radiation and cloud radiative properties in the ECMWF operational weather forecast model. *J Geophys Res* 96: 9121–9132
- Palmer TN, Anderson DLT (1994) The prospects for seasonal forecasting – A review paper. *Q J R Meteorol Soc* 120: 755–793
- Palmer TN, Mansfield DA (1986) A study of wintertime circulation anomalies during past El Niño events using a high resolution general circulation model. I: influence of model climatology. *Q J R Meteorol Soc* 112: 613–638
- Pan Y-H, Oort AH (1983) Global climate variations connected with sea surface temperature anomalies in the eastern equatorial Pacific Ocean for the 1958–73 period. *Mon Weather Rev* 111: 1244–1258
- Philander SG (1990) El Niño, La Niña, and the Southern Oscillation. Academic Press, 289 pp
- Phillips TJ (1994) A summary documentation of the AMIP models. PCMDI Rep 18, PCMDI, Lawrence Livermore National Laboratory, California, 343 pp
- Rasmusson EM, Carpenter TH (1982) Variations in tropical sea surface temperature and surface wind fields associated with the Southern Oscillation/El Niño. *Mon Weather Rev* 110: 354–384
- Reynolds RW, Marsico DC (1993) An improved real-time global sea surface temperature analysis. *J Clim* 6: 114–119
- Sardeshmukh PD, Hoskins BJ (1988) The generation of global rotational flow by steady idealized tropical divergence. *J Atmos Sci* 45: 1228–1251
- Simmons AJ, Burridge DM, Jarraud M, Girard C, Wergen W (1988) The ECMWF medium-range prediction models, development of the numerical formulations and impact of the increased resolution. *Meerol Atmos Phys* 40: 28–60
- Slingo JM, Sperber KR, Boyle JS, Ceron J-P, Dix M, Dugas B, Ebisuzaki W, Fyfe J, Gregory D, Gueremy J-F, Hack J, Harzallah A, Inness P, Kitoh A, Lau K-M, McAvaney B, Madden R, Matthews A, Palmer TN, Park C-K, Randall D, Renno N (1996) Intraseasonal oscillations in 15 atmospheric general circulation models. *Clim Dyn* 12: 325–357
- Shukla I, Gutzler DS (1983) Interannual variability and predictability of 500 mb geopotential heights over the Northern Hemisphere. *Mon Weather Rev* 111: 1273–1279
- Tiedtke M (1989) A comprehensive mass-flux scheme for cumulus parametrization in large-scale models. *Mon Weather Rev* 117: 1779–1800
- Tiedtke M, Heckley WA, Slingo JM (1988) Tropical forecasting at ECMWF: The influence of physical parametrization on the mean structure of forecasts and analyses. *Q J R Meteorol Soc* 114: 639–664
- Ting M, Sardeshmukh PD (1993) Factors determining the extratropical response to equatorial diabatic heating anomalies. *J Atmos Sci* 50: 907–918
- Thompson SL, Pollard D (1995) A global climate model (GENESIS) with a land-surface transfer scheme (LSX). Part I: present climate simulation. *J Clim* 8: 732–761



- Trenberth KE (1992) Global analyses from ECMWF and Atlas of 1000 to 10 mb circulation statistics. NCAR Tech Note, NCAR/TN-373 + STR, 191 pp
- Trenberth KE, Olson JG (1988) An evaluation and intercomparison of global analyses from the National Meteorological Center and the European Centre for Medium Range Weather Forecasts. *Bull Am Meteorol Soc* 69:1047–1057
- van Loon H, Madden RA (1981) The Southern Oscillation. Part I: global associations with pressure and temperature in northern winter. *Mon Weather Rev* 109:1150–1162
- Wallace JM, Gutzler DS (1981) Teleconnections in the geopotential height field during the Northern Hemisphere winter. *Mon Weather Rev* 109:784–812
- Wang W-C, Shi G-Y, Kiehl JT (1991) Incorporation of the thermal radiative effect of CH<sub>4</sub>, N<sub>2</sub>O, CF<sub>2</sub>Cl<sub>2</sub>, and CFCl<sub>3</sub> into the National Center for Atmospheric Research Community Climate Model. *J Geophys Res* 96:9097–9103
- Wang W-C, Liang X-Z, Dudek MP, Pollard D, Thompson SL (1995) Atmospheric ozone as a climate gas. *Atmos Res* 37:247–256
- Wu X, Yanai M (1994) Effects of vertical wind shear on the cumulus transport of momentum: observations and parametrization. *J Atmos Sci* 51:1640–1660
- Zebiak S, Cane M (1987) A model El Niño/Southern Oscillation. *Mon Weather Rev* 115:2262–2278
- Zwiers FW (1987) A potential predictability study conducted with an atmospheric general circulation model. *Mon Weather Rev* 115:2957–2974